AL-TR-89-054 AD:

Final Report
for the period
September 1988 to
May 1989

System Identification Tools for Control Structure Interaction

January 1990

Authors:
R.L. Kosut
G.M. Kabuli

Integrated Systems Inc.
2500 Mission College Blvd.
Santa Clara CA 95054-1215

DTIC
ELECTE
MAR 28 1990
S B D

Approved for Public Release

Prepared for the: **Astronautics Laboratory (AFSC)**
Air Force Space Technology Center
Space Systems Division
Air Force Systems Command
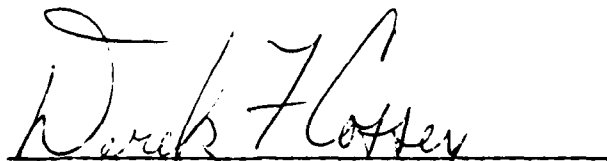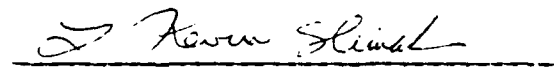Edwards Air Force Base, CA 93523-5000

NOTICE

When U.S. Government drawings, specifications, or other data are used for any purpose other than a definitely related Government procurement operation, the fact that the Government may have formulated, furnished, or in any way supplied the said drawings, specifications, or other data, is not to be regarded by implication or otherwise, or in any way licensing the holder or any other person or corporation, or conveying any rights or permission to manufacture, use, or sell any patented invention that may be related thereto.
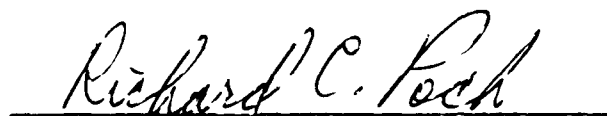
FOREWORD

This final report was submitted Integrated Systems Inc., Santa Clara CA on completion of SBIR contract F04611-89-C-0006 to the Astronautics Laboratory (AFSC), Edwards Air Force Base, CA. AL Project Manager was Lt Derek Cossey.

This report has been reviewed and is approved for release and distribution in accordance with the distribution statement on the cover and on the DD Form 1473.

DEREK F. COSSEY, 2Lt, USAF
Project Manager

L. KEVIN SLIMAK
Chief, Subsystems Branch

FOR THE DIRECTOR

RICHARD C. POCH, Lt Col, USAF
Deputy Director, Aerospace
Vehicle Systems Division

REPORT DOCUMENTATION PAGE

Form Approved
OMB No. 0704-0188

1a. REPORT SECURITY CLASSIFICATION UNCLASSIFIED	1b RESTRICTIVE MARKINGS
2a. SECURITY CLASSIFICATION AUTHORITY	3. DISTRIBUTION/AVAILABILITY OF REPORT Approved for Public Release;
2b. DECLASSIFICATION/DOWNGRADING SCHEDULE	Distribution is unlimited

4. PERFORMING ORGANIZATION REPORT NUMBER(S) ISI Report 7801-01	5. MONITORING ORGANIZATION REPORT NUMBER(S) AL-TR-89-070

6a. NAME OF PERFORMING ORGANIZATION Integrated Systems Inc.	6b. OFFICE SYMBOL (If applicable)	7a. NAME OF MONITORING ORGANIZATION Astronautics Laboratory (AFSC)
6c. ADDRESS (City, State, and ZIP Code) 2500 Mission College Boulevard Santa Clara CA 95054-1215		7b. ADDRESS (City, State, and ZIP Code) AL/VSSS Edwards AFB CA 93523-5000

8a. NAME OF FUNDING/SPONSORING ORGANIZATION	8b. OFFICE SYMBOL (If applicable)	9. PROCUREMENT INSTRUMENT IDENTIFICATION NUMBER F04611-89-C-0006

8c. ADDRESS (City, State, and ZIP Code)	10. SOURCE OF FUNDING NUMBERS

	PROGRAM ELEMENT NO.	PROJECT NO.	TASK NO	WORK UNIT ACCESSION NO.
	65502F	2864	00	44

11. TITLE (Include Security Classification)

System Identification Tools for Control Structure Interaction (U)

12. PERSONAL AUTHOR(S)
Kosut, Robert L.; Kabuli, Guntekin M.

13a. TYPE OF REPORT Final	13b. TIME COVERED FROM 8809 TO 8905	14. DATE OF REPORT (Year, Month, Day) 9001	15. PAGE COUNT 96

16. SUPPLEMENTARY NOTATION

17. COSATI CODES			18. SUBJECT TERMS (Continue on reverse if necessary and identify by block number)
FIELD	GROUP	SUB-GROUP	Flexible space structures, on-orbit identification, dynamics,
22	01		system identification, robustness, dynamic modeling, robust
22	02		control design, control design procedure

19. ABSTRACT (Continue on reverse if necessary and identify by block number)

To meet the stringent closed-loop performance specifications of flexible space structures will require very accurate dynamical models for control design. Ground-testing is not likely to produce the on-orbit dynamics to within the requisite accuracy. This report examines the feasibility of on-orbit identification for robust control design. A simulation model of the ASTREX facility is used as a testbed. It is demonstrated that robust control design can be used to dictate the accuracy requirements of on-orbit identification. It is also shown that prior knowledge of the system dynamics together with on-orbit data can lead to an estimate of a frequency dependent uncertainty profile associated with an identified model. These methodologies are necessary for an on-orbit adaptive robust control design procedure.

20. DISTRIBUTION/AVAILABILITY OF ABSTRACT ☒ UNCLASSIFIED/UNLIMITED ☐ SAME AS RPT. ☐ DTIC USERS	21. ABSTRACT SECURITY CLASSIFICATION UNCLASSIFIED	
22a. NAME OF RESPONSIBLE INDIVIDUAL DEREK F. COSSEY, 2Lt, USAF	22b. TELEPHONE (Include Area Code) (805) 275-5350	22c. OFFICE SYMBOL AL/VSSS

DD Form 1473, JUN 86 *Previous editions are obsolete.*

Contents

i

List of Tables

List of Figures

1 Introduction

Many planned Air Force missions require precise slewing and pointing control of large flexible structures in space. Success of these missions depends critically on achieving and maintaining highly precise (nano radian) pointing control of line-of-sight over the duration of the entire mission. Typical missions include surveillance, communications, target detection, weapon pointing and tracking.

Space structures are subject to disturbances of bandwidths that require control of many structural modes. To enable high performance control of these in-band modes requires a good model of the structure. Unfortunately, models based on physical and/or manufacturing data do not have the requisite accuracy. Model inaccuracies arise from many sources, *e.g.*, changes in mechanical properties due to manufacturing variations, assembly variations, effect of radiation, plasma and temperature, and so on. Even small variations can have significant negative effects on closed-loop performance. If the control is made robust to these inaccuracies by treating them as model uncertainties, the resulting control performance is often orders of magnitude worse than the mission requirements. System identification reduces these model inaccuracies so that high control performance can be achieved in the presence of model variations.

Advances in Control Structure Interactions (CSI), based on experience from programs such as ACOSS and VCOSS [1] and R2P2 [2], have clearly demonstrated the importance of system identification in achieving high performance control (see Table 1).

Table 1: Performance depends on model accuracy.

Model Information	Performance
NASTRAN + manufacturing tolerances	unstable
NASTRAN + ground testing	unstable to 50% performance degradation
on-orbit identification	meets performancce

Prior to 1983, all work in system identification for CSI was performed using non-standard custom software or spectral analyzers. Since then a number of tools have emerged for system identification [18,9]. These tools have proven to be very valuable for off-line SISO system identification, but mostly in research environments in the hands of experts in system identification. Current software tools, such as $MATRIX_x$, contain primitives which implement certain identification methods. Several of these tools have been investigated under Phase I and have proven to be reliable.

To design a feedback system, the control engineer typically requires knowledge of the system transfer function along with a frequency dependent uncertainty profile. Typically, the model is very accurate over the bandwidth of interest, and can be considerably inaccurate outside of this range. To understand more fully the needs of system identification for control design, it is necessary to fully understand the control design requirements.

1.1 Organization of Report

Section 2 focuses on the identification issues related to the ASTREX model as described in Section 3.2 . One of the cross-channel transfer functions is identified by least-squares estimation, using simulation data from the ASTREX model. The model errors introduced are within the stability margin of the closed-loop LAC/HAC system in Section 5 .

Section 3 introduces the plant description and the design assumptions that are made in order to obtain the model used in the LAC/HAC designs.

Colocated rate-feedback and its limitations are discussed in Section 4 . Improved disturbance attenuation is achieved by the $\mathcal{H}_\infty$ high-authority control designs. Section 5 discusses high-authority controller design with no LOS measurement and Section 6 shows the effect of using LOS measurements.

2 System Identification for Control Design

2.1 Control Structure for LSS

As demonstrated in the ACOSS and VCOSS programs [1], a two-level control architecture consisting of active feedback control and rate damping mechanisms (active or passive) is a practical necessity for LSS control.
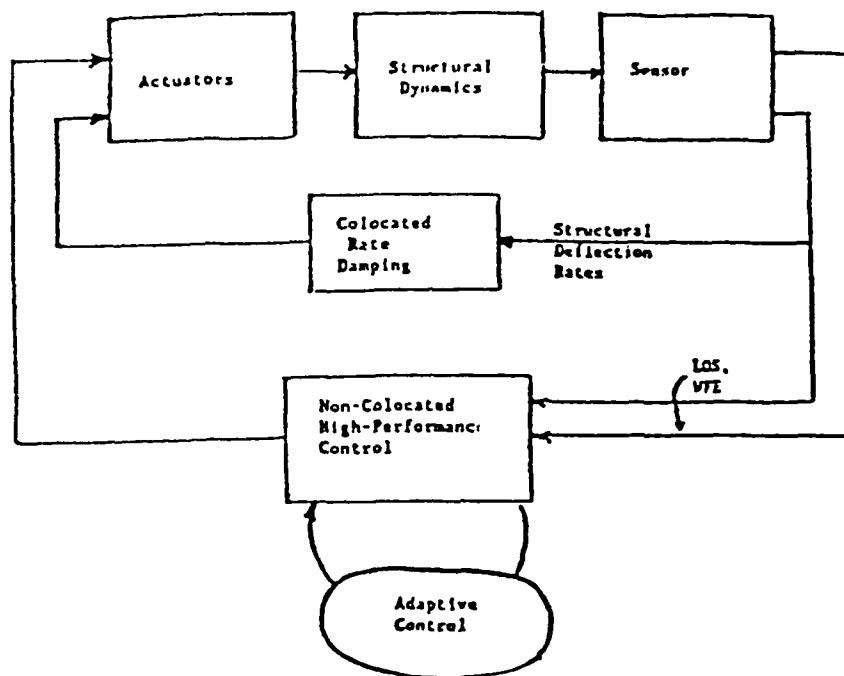
Figure 1: Two-Level Control Architecture

The basic two-level control architecture is depicted in **Figure 1**. The two levels consist of rate damping mechanisms, typically colocated, and a high performance controller, typically non-colocated. The colocated controller consists of active and/or passive rate damping devices placed at critical structural locations, and their design requires only a coarse knowledge of system dynamics. This is an inherently robust controller, but yields low performance, and has been referred to as the low authority control (LAC) system. The high performance controller is non-colocated and requires an accurate knowledge of critical modes, and hence, is very sensitive to structural parameter variations. This controller, referred to as the high authority control (HAC) system, provides high damping and mode shape adjustment in selected modes in order to meet the performance demands. The synthesis and design of the HAC/LAC system has to be properly integrated to avoid performance degradation due to modeling inaccuracies, [4]. With this architecture, as shown in Figure 1, only the HAC-system is likely to be tuned by an adaptive system, (via

3

on-orbit system identification and control re-design). The LAC system, due to colocation, provides significant robustness to parameter variations, but the performance increase over the open loop structure is moderate. The opposite is true for the HAC system, which provides significant performance increase, but is very sensitive to parameter variations. Adaptive control of the HAC system (*i.e.* , system identification and control re-design) allows for a much wider latitude in parameter variation while maintaining the performance level required.

The two-level design is usually done in two stages. First the LAC system is designed to achieve some reasonable damping levels in critical performance variables, *e.g.* , line-of-sight error and actuator authority. The number of colocated actuators for a LAC system vary depending upon the type of actuator, but typical numbers are from 10 to 50. "Smart structures" which have imbedded piezo-electric and (possibly) semi-conductor material can be thought of as distributed rate damping mechanisms, but still with low authority. Design methods can be based on trial and error on some parameter optimization.

After the LAC design is complete, then the HAC is designed using the LAC system already included in the design model. The HAC system uses a small number of actuators and sensors usually corresponding to the important degrees of freedom in the line-of-sight error, say from 3 to 6 inputs and outputs. Methods for HAC design are typically multivariable methods such as $\mathcal{H}_2$ or $\mathcal{H}_\infty$ approaches, *e.g.* , [15,8]. In Sections 4 and 5 , we describe in detail a HAC/LAC design for the ASTREX model. The LAC is designed based partly on trial and error and the HAC is designed using $\mathcal{H}_\infty$ methods.

2.2 Accuracy of Identified Model

Suppose we wish to identify the transfer matrix from the HAC inputs to the measured outputs. From Section 3.2 , the HAC actuators are chosen as proof mass actuautors at nodes 100x and 100y, with colocated velocity sensors. Using the nominal ASTREX model, gain and phase plots of the four transfer functions from $(f100x, f100y)$ to $(v100x, v100y)$, under LAC, are shown in Figure 2.

4
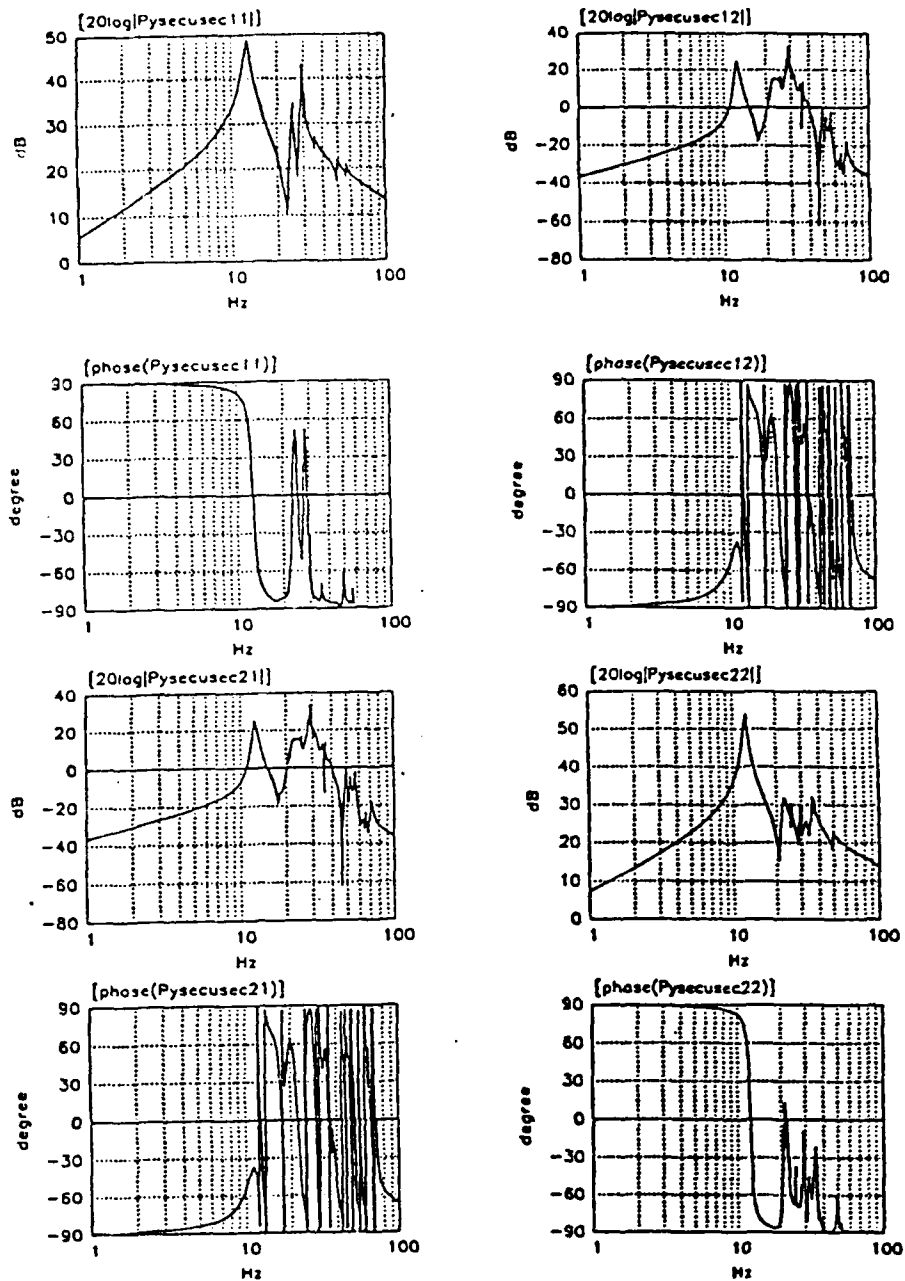
Figure 2: Gain/phase plots of $(f100x, f100y)$ to $(v100x, v100y)$ under LAC.

5

Suppose that each of the four transfer functions is perturbed by distinct stable transfer functions, each with the same frequency bound. Using the nominal model with the HAC/LAC design described in Section 5 yields the stability margin[1] shown in Figure 3. This margin is precisely the maximum bound on the above perturbations for which the HAC/LAC system can maintain stability.
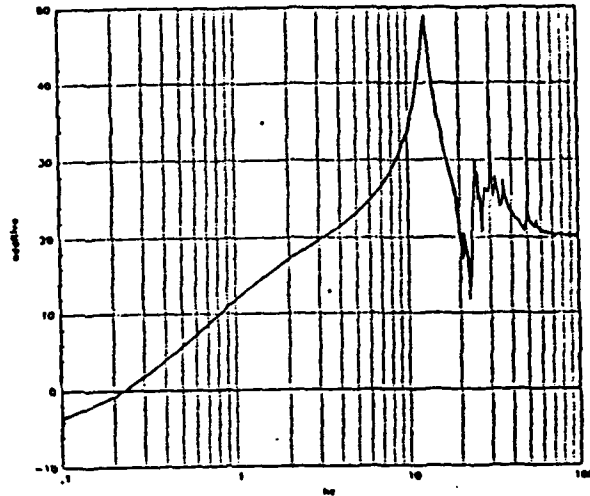
Figure 3: Stability margin to additive perturbations.

In terms of system identification, the margin is precisely the amount of admissible error between the nominal system and any identified model. Put another way, as long as the model error is below the margin, the closed loop system will remain stable.

In the next section we discuss some methods of system identification and compare the results to the margin in Figure 3.

2.3   Parametric Transfer Function Estimation

The estimation of a system's transfer function from input-output data has, of course, a long history, and we will not attempt to document that here. There are many excellent survey articles and textbooks that can be referenced, e.g. , [24,19,16,10,9]. These references clearly explain the theory and practice of both parametric and non-parametric methods of transfer function estimation.

In this section we describe the Phase I results with the basic tools for parametric transfer function estimation. The emphasis throughout the discussion is on LSS and we use

---

[1]The stability margin is the amount by which the actual system frequency response can differ from the design model and still maintain stability. There are at present several algorithms which compute various good approximations of the margin. These are contained in the new MATRIX$_x$ Robust Control Module and their application to the ASTREX model is described in Section 5 .

a linear state-space model of the ASTREX facility to illustrate the tools and requirements. Non-parametric methods are discussed in Section 2.6.

2.3.1 Prediction Error Models

Parametric methods of identification proceed by first selecting a set of discrete-time candidate models of the form[2]

$$y \;=\; G_\theta u + v \tag{1}$$
$$v \;=\; H_\theta e \quad , \tag{2}$$

where $e(t)$ is an "unpredictable" but bounded sequence; θ is a vector of model parameters, $u(t)$ and $y(t)$ are the measured input and output, respectively. The above model form is quite general; $G_\theta(z)$ is the input/output transfer function, and $H_\theta(z)$ represents the noise dynamics, $e.g.$, if $e(t)$ is a zero-mean white noise sequence of intensity λ, then $v(t)$ has spectral density

$$S_{vv}(\omega) = \lambda |H_\theta(e^{j\omega})|^2 \quad . \tag{3}$$

The dependence of the transfer functions G_θ and H_θ on the parameter vector θ is intimately related to the modeling process. If the models arise from physical considerations, then the parameters have a physical meaning, $e.g.$, mass, stiffness, and so on. Often, canonical models are used where the parameters are simply taken as coefficients in a transfer function. In the former case there are fewer parameters but these enter into the transfer function coefficients in a complicated manner. In the latter case there are more parameters to learn, but they enter the model in a simple manner, thereby reducing the computational burden.

Assuming that $e(t)$ is white noise, the best prediction of $y(t)$, given the data up to $t-1$, is

$$\hat{y}_\theta = H_\theta^{-1} G_\theta u + (1 - H_\theta^{-1}) y \quad . \tag{4}$$

The transfer matrix from (y, u) to $\hat{y}_\theta$ as defined by the above expression is referred to as the *one-step ahead predictor*. Hence, the *prediction error* is

$$\varepsilon_\theta \;=\; y - \hat{y}_\theta \tag{5}$$
$$=\; H_\theta^{-1}(y - G_\theta u) \quad . \tag{6}$$

Some examples of this model structure include the equation error model and the output error model.

---

[2]Discrete-time modeling is natural for identification because data is usually sampled. The standard notation is to normalize both the time t and the frequency ω with respect to the sampling time t_{sa}. Thus, t takes on only integer values and ω is restricted from $-\pi$ to π radians. Then, time in seconds $= t \cdot t_{sa}$ and frequency in rad/sec $= \omega/t_{sa}$.

Equation Error Model Certainly one of the most widely used parametric models is the *equation error model*

$$A_\theta y = B_\theta u + e \quad,$$

where

$$
\begin{aligned}
B_\theta(z) &= b_1 z^{-1} + \cdots + b_n z^{-n} \\
A_\theta(z) &= 1 + a_1 z^{-1} + \cdots + a_n z^{-n} \\
\theta^T &= (a_1 \cdots a_n\, b_1 \cdots b_n) \quad.
\end{aligned}
$$

In terms of the general model structure

$$G_\theta = \frac{B_\theta}{A_\theta} \quad ; \quad H_\theta = \frac{1}{A_\theta} \quad.$$

Hence, the prediction error is

$$\varepsilon_\theta(t) = y(t) - \theta^T \phi(t)$$

with $\phi(t)$, the *filtered regression vector*, given by

$$\phi^T(t) = [-y(t-1) \cdots -y(t-n)\, u(t-1) \cdots u(t-n)] \quad.$$

A significant feature of this model is that the prediction error is affine in the parameter vector θ. Thus, convex functions of the prediction error, such as least-squares, have a unique global minimum.

Output Error Model In this case the parametric model has the form

$$y = \frac{B_\theta}{A_\theta} u + e \quad,$$

The prediction error is now

$$\varepsilon_\theta(t) = y(t) - \theta^T \phi_\theta(t) \quad,$$

where the regressor now depends on θ as follows,

$$\phi_\theta^T(t) = [-\hat{y}_\theta(t-1) \cdots - \hat{y}_\theta(t-n)\, u(t-1) \cdots u(t-n)]$$

and where $\hat{y}_\theta$ is the one-step ahead prediction of y based on the model, that is,

$$\hat{y}_\theta = \frac{B_\theta}{A_\theta} u \quad.$$

In terms of the general model structure,

$$G_\theta = \frac{B_\theta}{A_\theta} \quad ; \quad H_\theta = 1 \quad.$$

Unlike the equation error model, the prediction error is not affine in θ, but rather, is linear fractional. Convex funtions of the prediction do not necessarily have global minimum, and in fact, there can be local minima in disconnected convex sets in parameter space.

2.3.2 Least-Squares Criterion

Practically every parameter estimation scheme is based on developing an on-line or off-line procedure for selecting the model parameters θ so as to minimize some function of the prediction error $\varepsilon_\theta(t)$. For example, the *least-squares prediction error* estimate is

$$\hat{\theta}_N = \arg\min_\theta V_N(\theta) \tag{7}$$

with

$$V_N(\theta) = \frac{1}{N} \sum_{t=1}^{N} (F\varepsilon_\theta)(t)^2 \tag{8}$$

where $F(z)$ is a stable *data filter*. Techniques for computing $\hat{\theta}_N$ involve either iterative or recursive algorithms, see, *e.g.*, [10,9].

Using the equation error model structure together with the least-squares criteria leads to what is universally, but incorrectly, referred to as the "least-squares estimate". Specifically, the estimate can be obtained in closed form as

$$\hat{\theta}_N = \left[\sum_{t=1}^{N} (F\phi)(t)(F\phi)(t)^T \right]^{-1} \sum_{t=1}^{N} (F\phi)(t)(Fy)(t) \quad . \tag{9}$$

The indicated inverse exists if the inputs are *persistently exciting*, that is, they contain a sufficient number of distinct spectral lines, usually the order of the parametric model. The popularity of the this parameter estimator is principally due to the ease of obtaining a closed form solution. However, great care must be exercised when computing this for even as few as 5 parameters. Numerical difficulties can create havoc here. Fortunately much is known about how to obtain the least-squares estimate rapidly as well as accurately from the numerical standpoint. Current numerical algorithms use a singular value decomposition and are extremely accurate, *e.g.*, MATRIX$_X$. Recursive versions of the computation involve square-root algorithms, which are not quite as accurate, but are much faster. At present there are some recursive algorithms using singular values, which are still under investigation by many research groups.

2.3.3 Example of Least-Squares Estimation

During Phase I we investigated the least-squares (equation error) estimator using data from the ASTREX model described in Section 3.2 . The model contains 60 states (30 modes) from about 12 to 70 hz. We will try to identify one of the cross channel transfer functions shown in Figure 2, specifically the transfer function from an applied force (torque) at node 100 in the x-direction (labeled f100x) to a velocity measurement at node 100 in the y-direction (labeled v100y). To illustrate the issues we chose to find a model over the frequency range up to 35 hz[3]. The sampling frequency is chosen as 200

---

[3]In Section 6 , where the line-of-sight measurement was also used in feedback, the two-mode model consisting of the first two modes (12.2 and 12.6 Hz) was used to achieve a satisfactory $\mathcal{H}_\infty$ -design; hence, 35 Hz range was not applicable for this design. However, the design in Section 5 , where the line-of-sight measurement is not used in feedback, relies on an 11-mode model description up to 30 Hz range.

hz (more than 5 times the bandwidth of interest) and we take 4096 samples of the input and output. The input applied at f100x, referred to as u_{swp}, is a linear sine-sweep of unit magnitude from 1hz to 35 hz over about 20 sec. Figure 4 shows the time response of the measured output, referred to as y_{swp}, plotted against the sine-sweep frequency. Observe the oscillations at the modal frequencies.
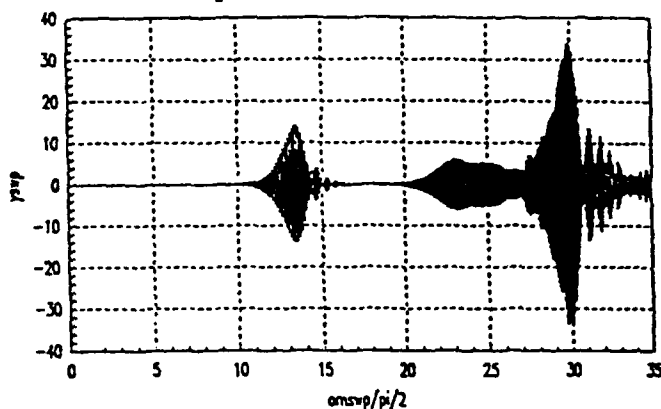
Figure 4: Measured output from sine-sweep input.
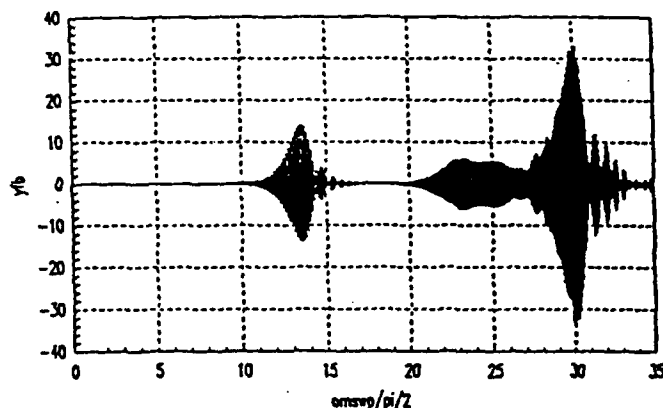
Figure 5: Filtered measured output from sine-sweep input.
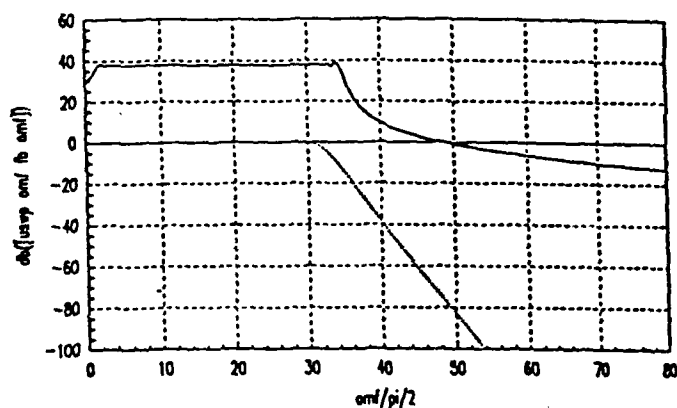
Figure 6: DFT of input sine-sweep and filter gain.

To emphasize our interest in the limited bandwidth, the data is filtered using a 16th order low pass Butterworth digital filter with a cutoff frequency of 32 hz. Figure 5 shows

the effect of the filter on the output response and Figure 6 displays the magnitude of the DFT (discrete Fourier transform) of the input u_{swp} and the filter.

The least- squares estimate using the filtered data is computed for two model orders: $n = 12$ (6 modes) and $n = 28$ (14 modes). In the 32 hz bandwidth of the data filter, there are actually 9 modes. Figures 7 and 8 show the magnitudes of the identified and true ASTREX model for the 6 mode and 14 mode case, respectively. They both seem to do a respectible job up to about 30 hz with the 14 mode model having the better fit at lower frequencies, as one might expect.
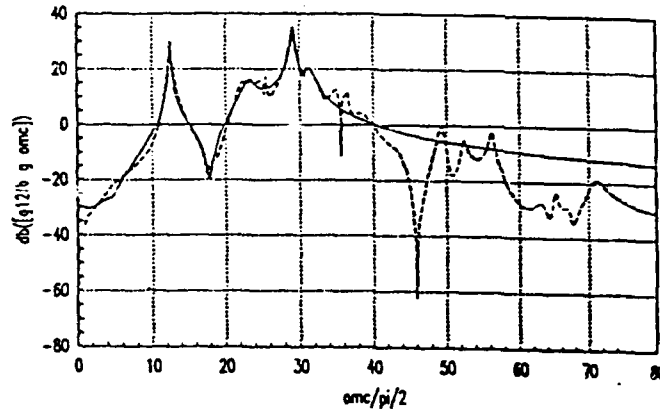
Figure 7: Frequency response magnitude of 6 mode id model from filtered data (dark line) compared to true system magnitude (dashed line).
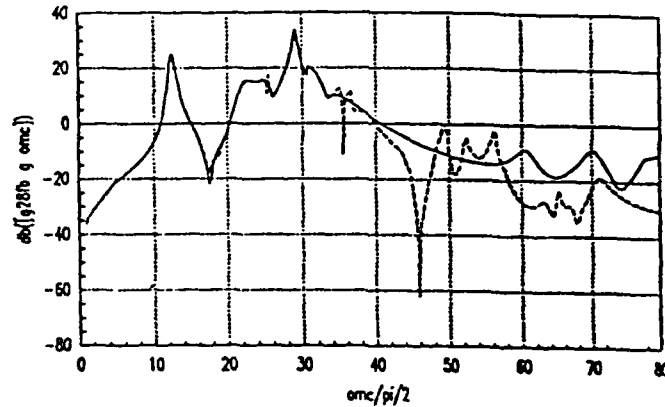
Figure 8: Frequency response magnitude of 14 mode id model from filtered data (dark line) compared to true system magnitude (dashed line).

Figures 9 and 10 show a comparison, in the frequency domain, of model error from the above two identified models of the ASTREX. The dark plots in both figures show the magnitude, in decibels (db), of the error between the identified model and the true but unknown system. The dashed plot is the level of allowable model error from Figure 3 , i.e., the stability margin. Observe that the model error in both cases falls below the margin at each frequency. Hence, stability is maintained if the control system were designed using either the 6 mode or 14 mode identified model. This may be at first surprizing, but this

11
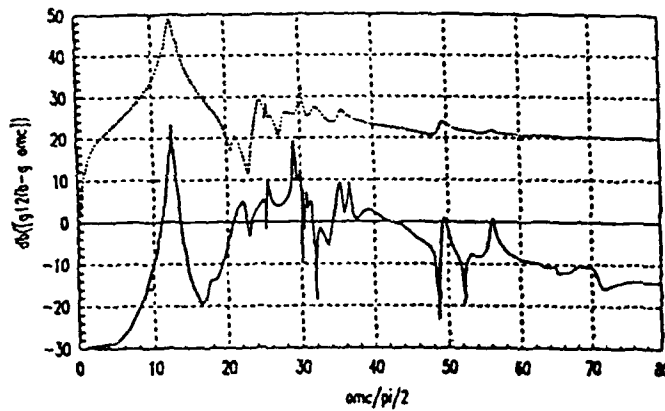
Figure 9: Dark line: frequency response magnitude in db of error between *true system* and the 6 mode id model from filtered data; Dashed line: stability margin from Figure 3.
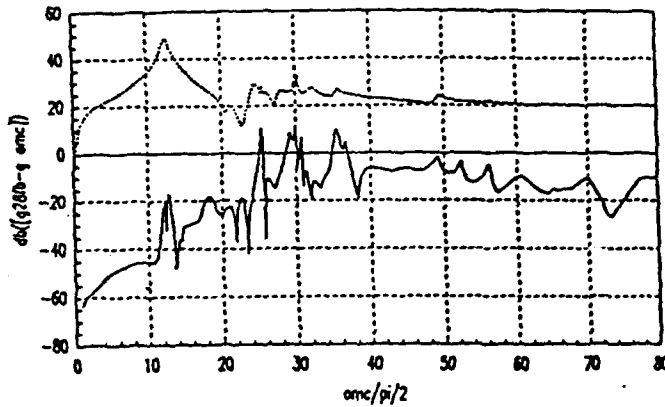
Figure 10: Dark line: frequency response magnitude in db of error between true system and the 14 mode id model from filtered data; Dashed line: stability margin from Figure 3.

phenomena is exactly in the nature of control design. It is not order of the model that counts, but rather, model accuracy over the bandwidth of interest. Beyond that bandwidth the controller must "roll-off" sufficiently fast so as not to interact with higher frequency modes.

The plots in Figure 9 also reveal that performance levels of attenuation will not be identical for both identified models. The small gaps between the 6 mode model and the margin in the 20-25 hz range can cause some significant performance degradation (see Section 5) .

If higher levels of attenuation are needed for this frequency range or beyond 25 hz, then it is necessary to either identify a model to capture that range, or else re-design the controller for a reduced performance level.

12

2.4 Experiment Design

The equation error model structure is a popular choice because it leads to a closed form solution of the least-squares estimation problem. But there are some pitfalls which can be avoided by proper selection of the experiment design variables. Some important design variables include:

- choice of parametric model structure

- choice of probing or test inputs

- choice of data filter

- choice of feedback (during experiment)

- choice of minimization criteria

- choice of computation method   .

To see some of the ways in which the above choices affect the identification outcome. let us continue with the least-squares equation error estimator. It can be shown [9] that for sufficiently large N, the least squares criterion

$$\sum_{t=1}^{N}(F\varepsilon_\theta)(t)^2 \approx \sum_{\omega \in \Omega} |(FAU_N)(\omega)|^2 \cdot |G(e^{j\omega}) - \frac{B(e^{j\omega})}{A(e^{j\omega})}|^2 + |(FAV_N)(\omega)|^2 \qquad (10)$$

where $U_N(\omega)$ and $V_N(\omega)$ are the discrete Fourier transforms (DFT) of u and the output disturbance v, respectively. The frequency set Ω consists of the (normalized DFT) frequncies $\{\omega_k = 2\pi k/N : k = 0, \ldots, N-1\}$.

The above expression shows a clear frequency domain interpretation of least- squares. What happens is that the parametric model B/A tries to fit the true system G in accordance with a "weighting function" $|FAU_N|$. Good frequency response fits are obtained where the weight is large. If the weight is large at high frequencies, where the noise term $|V_N|$ is present, then the identified model will be "biased" at high frequencies. Clearly the filter, if carefully selected, can easily offset this natural tendency of least-squares.

2.4.1 Choice of Data Filter

To verify this interpretation, we ran another experiment using the same sine-sweep input and process the data using least-squares but without the filter. We know that the filter makes little difference if the system is noise-free, which is unrealistic for CSI. Thus, we simulated a disturbance at the the input actuation nodes using a white noise whose intensity is 10% of the magnitude of the input sweep. This noise roughly approximates a disturbance due to coolant flow in the secondary mirrors.

Figure 11 shows the magnitude plot of the model error between true system and identified model with no data filter and the noise input active. Compare this with Figure 10,

13

which is obtained with the data filter. Observe how the identified model obtained from the unfiltered noisy data has significant errors at high frequencies.
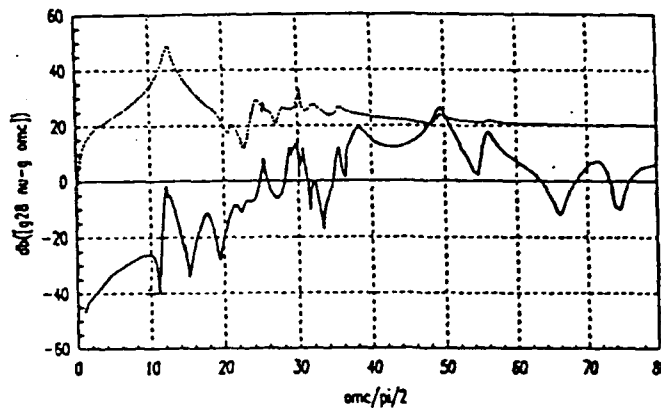
Figure 11: Dark line: frequency response magnitude in db of error between true system with noisy input and the 14 mode id model from unfiltered data; Dashed line: stability margin from Figure 3.

What happens in the unfiltered noisy case is that the identified model tries to fit the noise at high frequency, and hence, the low frequency model, which is important for control design, suffers. In fact, Figure 11 shows that at about 48 hz the model error magnitude crosses above the stability margin, and hence, closed-loop stability cannot be guaranteed using this model.

To further understand this phenomena, Figure 12 shows db plots of the frequency dependent weighting function $|(FAU_N)(\omega)|$ from (10) for three of the identified models. The two lower plots, which practically overlap, reflect two 14 mode identified models, both with data filtering but one has a noise added to the input. The upper plot relects the weight of the 14 mode identified model with no data filtering and with noise at the input. Observe that at high frequencies the lack of the data filter causes the weight to be just about uniform over all frequencies. Hence, the identified model tries to equally fit the noise which tends to dominate at high frequencies.

2.4.2 Choice of Test Signal

In the simulation experiment we used a sine-sweep to cover the frequency range of interest. Another good wideband signal is a so-called PRBS (pseudo random binary signal). These have been used extensively in identification experiments for process plants, but for some reason have not found there way into the aerospace community. There is no particular technical reason, and in fact, the spectral charcterics of the PRBS are easier to control. The one drawback is generating the signal, and this requires a shift register.

Another important aspect of on-orbit identification is that the system will undergo a performance degradation during testing. This necessitates making the testing period as short as possible. Hence, the purposes of the test will also dictate the type of probing signals.

14
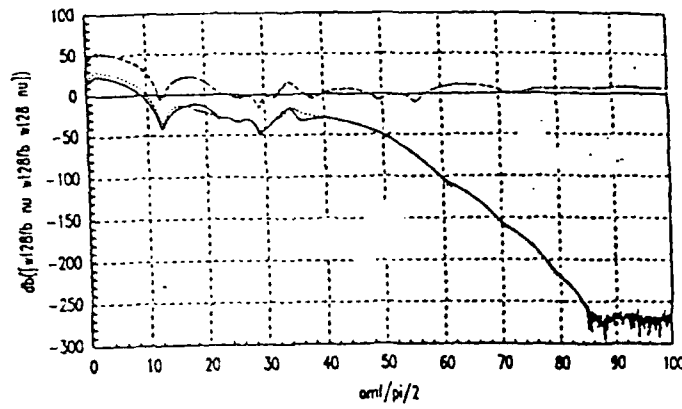
Figure 12: Plots of the weight $|(FAU_N)(\omega)|$ from (10). Lower plots: 14 mode id model with data filtering; one is noise free. Upper plot: 14 mode id model with noise and no data filter.

2.5 Model Error Estimation

In this section we address the issue of obtaining an estimate of the model error between an identified model and the system which actually generated the data. In the above example the true system is a simulation model, and hence, known by querry to the user. Thus it is possible when the simulation is available to obtain the *exact* error profile. This is very useful when one is performing analysis of the identification scheme.

When we turn to the situation of on-orbit identification, the true system is unknown, and then one has to rely on *a priori* or identified model. Prior knowledge of model errors which are typical for a class of identification experiments can be obtained from simulations which produce data like that shown in Figures 9 and 10. But it is also useful to obtain on-orbit estimates of the error to gain confidence in the identified model.

There are curently several approaches to this problem, and they can be broadly classified into parameter error estimation and frequency error estimation, *e.g.* , [20,21,22,26,23]. Here we will illustrate one of the frequency methods with the ASTREX data.

We use the method described in [22]. Form the output error

$$\hat{e} = \hat{y} - y$$

where $\hat{y}$ is the output of the identified transfer function

$$\hat{y} = \hat{G}u$$

Since the measured output obeys

$$y = Gu + v$$

it follows that

$$\hat{e} = \Delta u - v \qquad \Delta = \hat{G} - G$$

where Δ is the model error between the identified transfer function and the true but unknown transfer function. We seek to estimate $|\Delta(e^{j\omega})|$ or to find an upper bound. If u

15

and v are independent, then a simple bound is

$$\hat{\ell}(\omega) = \left| \frac{\hat{E}_N}{U_N} \right|$$

where $\hat{E}_N, U_N$ are the DFT's of $\hat{e}, u$, respectively. The DFT can be computed using a variety of methods involving choices of frequency and lag windows, batch frequency averaging methods, and so on, e.g. , [9].
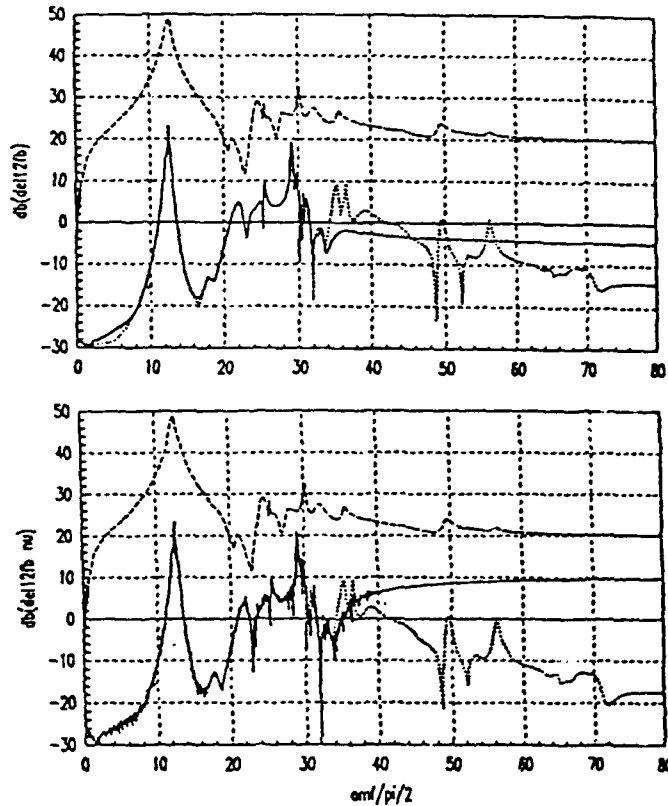
Figure 13: Model error for 6 mode identified model from filtered data. Upper: noise free, lower: noisy input. Solid lines: error estimate; dotted lines: true error; dashed lines: stability margin from Figure 3.

Figures 13 and 14 show the error estimates compared to the true errors for the 6 mode and 14 mode identified models discussed previously. The identified models are obtained using the data filter. Each figure shows the case with and without the input noise. Observe that in all cases the error estimate is quite accurate in the bandwidth of the filter; but there is a tendency to be inaccurate outside the band. This implies that some amount of prior knowledge should be used in the control design to exert caution at these frequencies. These results were obtained using the FFT function in MATRIX$_y$ with no data windows using the filtered data.

16
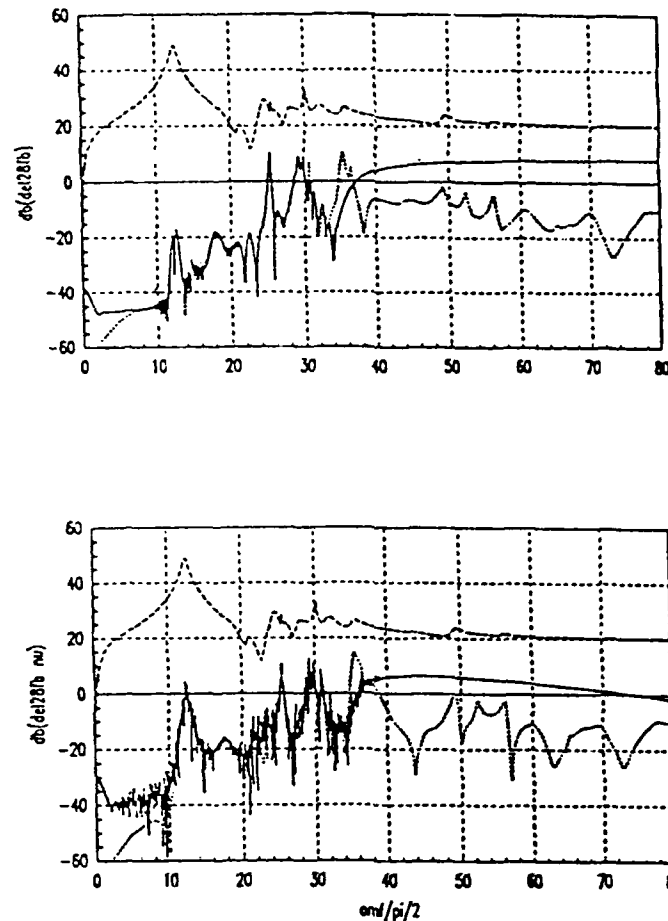
Figure 14: Model error for 14 mode identified model from filtered data. Upper: noise free, lower: noisy input. Solid lines: error estimate; dotted lines: true error; dashed lines: stability margin from Figure 3.

2.6 Nonparametric Transfer Function Estimation

In this section we briefly discuss two methods for estimation of a transfer function evaluated at many frequency points, namely, the correlation method and the spectral method. In both cases the assumption is that the system to be estimated is described as before, that is

$$y = Gu + v$$

where $G(z)$ is the unknown (discrete-time) transfer function. The measured data is

$\{y(t), u(t) : t = 1, \ldots, N\}$ where (y, u) are input and output sampled sequences, respectively. The sequence v is a disturbance or noise sequence as seen at the plant output. Although in general the input u could be the output of a feedback system, we will assume for now that it is an open-loop sequence supplied by the user. Hence, u is independent of the disturbance v. In addition, $G(z)$ is assumed to be stable, which of course is the case for LSS, although the damping is small.

17

In the next two sections we state some known results for evaluating the model error accrued by using these nonparametric methods.

2.6.1 Correlation Methods

In the correlation method the input is a single tone at frequency ω,

$$u(t) = \begin{cases} \alpha \cos \omega t & t \geq 1 \\ 0 & t \leq 0 \end{cases} \qquad 0 < \omega < \pi$$

The transfer function estimate at ω is then[4]

$$\ddot{G}_N(\omega) = \frac{2}{\alpha N} \sum_{t=1}^{N} y(t) e^{-j\omega t}$$

The estimator can be analyzed under the following assumptions:

1. Let $g(t)$ be the pulse response of $G(z)$, *i.e.* ,

$$G(z) = \sum_{t=1}^{\infty} g(t) z^{-t}$$

Since $G(z)$ is stable, there are constants $M \geq 1$ and $0 < \rho < 1$ such that

$$|g(t)| \leq M \rho^t$$

2. Let $v(t)$ be zero-mean sequence with spectral density $S_{vv}(\omega)$.

Under these conditions the following expressions can be obtained for the bias and variance of the estimate:[5]

Bias

$$|\mathcal{E}[\hat{G}_N(\omega) - G(e^{j\omega})]| \leq \frac{1}{N} \left[\frac{M\rho(1-\rho^N)}{(1-\rho)^2} + |G(e^{j\omega}) \frac{\sin N\omega}{\sin \omega}| \right]$$

Variance

As $N \to \infty$,

$$\mathcal{E}|\hat{G}_N(\omega) - \mathcal{E}\hat{G}_N(\omega)|^2 \approx \frac{4}{N} \frac{S_{vv}(\omega)}{\alpha^2}$$

Typically the frequencies ω of the correlation transfer function estimate are those of the DFT frequencies

$$\{\omega = \frac{k\pi}{N} : k = 0, \ldots, N-1\}$$

---

[4]If the input is a constant ($\omega = 0$), then the $2/N$ factor is replaced by $1/N$.

[5]These are typical results for any of a number of variations on the correlation method.

Hence, the term in the bias involving $\sin N\omega$ is zero and it is the first term which dominates the bias. This term is due to the transient in the system response to the sinusoidal input at frequency ω.

A useful measure of the error between the estimate and the true system is the meas-square-error (MSE)

$$\mathcal{E}|\hat{G}_N(\omega) - G(e^{j\omega})|^2 = \text{bias}^2 + \text{variance}$$

For large values of N the variance tends to dominate the bias contribution to the MSE. This is because the variance contribution contracts at a rate proportional to $1/N$ as compared to the (bias)^2 contraction of $1/N^2$. However, a small bias can only be had for a *very* large value of N, primarily because of the small inherent damping of the flexible structure. To illustrate this point, suppose there is no disturbances, thus $S_{vv}(\omega) = 0$, and let the true system be given by

$$G(s) = \frac{s}{s^2 + 2\zeta\Omega s + \Omega^2}$$

which represents one flexible mode from a co-located force input to velocity output. Using some values compatible with the ASTREX model let the modal frequency be 12 hz with a 2% damping, thus,

$$\Omega = 2\pi(12) \qquad \zeta = .002$$

Using the sampling frequency of 200 hz gives

$$M = .0049 \qquad \rho = .999246$$

Figure 15 shows the relative bias error upper bound

$$|\mathcal{E}\frac{\hat{G}_N(\omega) - G(e^{j\omega})}{G(e^{j\omega})}| \le \frac{1}{NG(e^{j\omega})}\left[\frac{M\rho(1-\rho^N)}{(1-\rho)^2}\right]$$

as a function of frequency for varying values of data points.
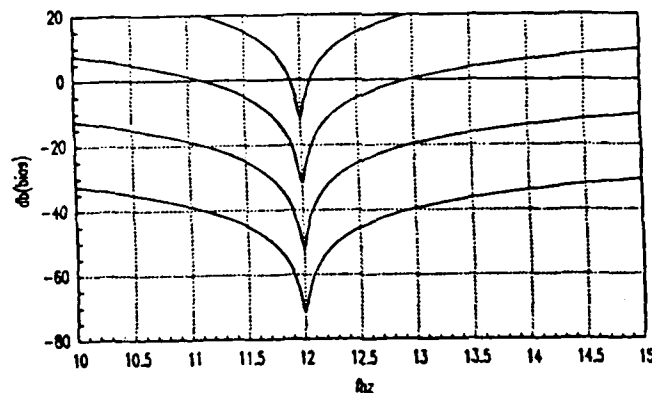
Figure 15: Bias in relative error vs. frequency for varying number of data points $N = 10^4, 10^5, 10^6, 10^7$.

The number of data points shown is for $N = 10^4, 10^5, 10^6, 10^7$. Since the sampling frequency is 200 hz, this corresponds to observation times of $T = 50$ sec, 8.33 min, 83.33

19

min, 13.89 hrs. The longer the observation times the smaller the error, which contracts of course at a rate of $1/N$. The plots are to be interpreted so that to acheive the indicated accuracy at the given frequency, it is necessary to dwell on that frequency for N sample times. As a result, to obtain at least a -40 db accuracy from 11 to 13 hz would require a significant percentage of a full days worth of data. Standard "wave analyzer" equipment is commercially available for this purpose. However, the time required to sequentially process all the data to obtain a given accuracy may not be necessary for the purposes of control design from on-orbit data. Moreover, the mission requirements may preclude this type of identification experiment.

2.6.2 Spectral Methods

Similar convergence properties as a function of data length can also be obtained by decomposing an arbitrary input into its spectral components, that is, spectral estimation methods. The standard techniques for spectral estimation involve data windowing in time and frequency, aligning, anti-aliasing filters, and many other proceedures which it is not possible to describe here. The details can be found in the previously mentioned references. However, as in the correlation methods, it is also possible here to obtain analytic expressions for the model error.

Spectral techniques estimate the frequency response $G(e^{j\omega})$ via

$$\hat{G}(\omega) = \frac{\hat{S}_{yu}(\omega)}{\hat{S}_{uu}(\omega)}$$

where $\hat{S}_{yu}(\omega)$ and $\hat{S}_{uu}(\omega)$ are estimates of the cross-spectrum and auto-spectrum, respectively. Observe that the frequency response is given precisley by

$$G(\omega) = \frac{S_{yu}(\omega)}{S_{uu}(\omega)}$$

where S_{yu} and S_{uu} are the actual spectra. Schemes for obtaining good sprectral estimates are based on convolving the DFT's of y, u with a *lag window* $W_\gamma(\omega)$. The window is essentially a frequency function whose shape is determined by the design parameter γ. The window serves to smooth the estimates obtained from the DFT. The window width is approximately $1/\gamma$, so as γ increases, the window becomes more narrow and vice versa.

For large values of N, the mean-square-error (MSE) of the estimate is [9]

$$\mathcal{E}\{|\hat{G}(e^{j\omega}) - G(e^{j\omega})|^2\} \approx M^2(\gamma)|R(\omega)|^2 + \frac{1}{N}L(\gamma)S_{dd}(\omega)/S_{uu}(\omega)$$

where

$$R(\omega) = G''(e^{j\omega}) + G'(e^{j\omega})S'_{uu}(\omega)/S_{uu}(\omega)$$

with $'$ and $''$ denoting differentiation with respect to ω, once and twice, respectively. Also

$$
\begin{aligned}
M(\gamma) &= \int_{-\pi}^{\pi} \omega^2 W_\gamma(\omega)\, d\omega \\
L(\gamma) &= \int_{-\pi}^{\pi} W_\gamma^2(\omega)\, d\omega
\end{aligned}
$$

20

Observe that as γ increases, $M(\gamma)$ decreases, and $L(\gamma)$ increases. Thus, as γ increases, the first term (the bias) decreases, but the second term (the variance) increases. Clearly for large N there is an optimal choice of lag window width to minimize the MSE for fixed N, and this can be calculated [9].

2.7   Summary of Identification Issues

At this point we can draw several conclusions as to what information is needed for identification:

- The user needs the stability margin associated with a nominal system model for control design.

- The user needs to display this information together with a model error profile from the identifi·d model.

- If the true system is not available and *a priori* information is inadequate, then the user needs to estimate the identified model accuracy from the data.

- If the above tests fail to convince the user that the nominal design has adequate robustness to identification errors, then the user needs some "expert" advice as to the next step. Or, in the case of an expert user, what is needed is easy access to a library of identification and control "design knobs".

3   Flexible Spacecraft Modeling

3.1   Modal Equations

The crucial information in the dynamic control of a physical system is an "adequate" model of the system for the desired performance specifications. Any compensator design methodology relies on this "model" (from now on, referred to as the plant); hence any idealization or simplification must be done with due care to have a plant that reasonably represents the physical system.

Programs such as NASTRAN and SPAR are the primary tools for generating dynamic models of conceptual spacecraft. Finite-element structural programs provide the control designers with a set of modal frequencies and a set of mode shapes (eigenvectors) corresponding to appropriate boundary values (e.g., free-free modes). A brief outline of the associated eigenproblem is given below.

A linear time-invariant finite-dimensional model of a flexible structure can be described as

$$M\ddot{q} \; + \; D\dot{q} \; + \; Kq \; = \; Fu \quad , \qquad (11)$$

where the mass matrix M is symmetric, positive-definite (i.e., all of the eigenvalues are positive) and the stiffness matrix K is symmetric positive semi-definite (i.e., all of the eigenvalues are nonnegative). The vector q in (11) consists of the modal translational- and rotational-displacements at each nodal station. The forcing matrix F is determined by the locations of exogenous forces or torques. In most cases the damping matrix D in (11) is not known, hence the undamped case

$$M\ddot{q} \; + \; Kq \; = \; Fu \qquad (12)$$

is transformed into a state-space form by a diagonalizing transformation and then, a damping ratio of $\zeta \ll 1$ is assigned to every mode. This procedure is now described.

Since the mass matrix M is real, symmetric, positive-definite, there exits a real unitary matrix U_M (i.e., $U_M^T U_M = I$) such that $M = U_M \Sigma_M U_M^T$ (the Schur decomposition of M), where the diagonal matrix Σ_M is positive-definite. Define the symmetric positive semi-definite matrix S as $S := \Sigma_M^{-1/2} U_M^T K U_M \Sigma_M^{-1/2}$. Let U_S be a unitary matrix such that $S = U_S \Omega^2 U_S^T$ where the diagonal matrix Ω^2 is positive semi-definite. Define the transformation matrix Φ as $\Phi := U_M \Sigma_M^{-1/2} U_S$. Then

$$\Phi^T M \Phi \; = \; U_S^T \Sigma_M^{-1/2} U_M^T U_M \Sigma_M U_M^T U_M \Sigma_M^{-1/2} U_S \; = \; I \;, \qquad (13)$$

$$\Phi^T K \Phi \; = \; U_S^T \Sigma_M^{-1/2} U_M^T U_M \Sigma_M^{1/2} U_S \Omega^2 U_S^T \Sigma_M^{1/2} U_M^T U_M \Sigma_M^{-1/2} U_S = \Omega^2 \; . \qquad (14)$$

Note that such a transformation Φ and Ω satisfy the eigenproblem

$$M \Phi \Omega^2 \; = \; K \Phi \quad .$$

The NASTRAN analysis supplies the matrices Ω and Φ satisfying equations (13) and (14), with

$$\Omega = \mathrm{diag}[\omega_1 \ldots \omega_n] \quad , \quad \omega_i \leq \omega_{i+1}$$
$$\Phi = [\phi_1 \ldots \phi_n] \quad ,$$

where ϕ_i is the mode shape corresponding to the ith modal frequency ω_i . Substituting the change of coordinates

$$q = \Phi \eta$$

in (12), and using (13-14), we obtain the modal equations

$$\ddot{\eta} + \Omega^2 \eta = \Phi^T F u \quad . \tag{15}$$

Assigning a uniform damping ratio $\zeta \ll 1$ to each of the modes in (15), a state-space description can be obtained as follows:

$$\dot{x} = A x + B u \quad ,$$

where

$$A := \begin{bmatrix} 0 & I \\ -\Omega^2 & -2\zeta\Omega \end{bmatrix} \quad , \tag{16}$$

$$B := \begin{bmatrix} 0 \\ \Phi^T F \end{bmatrix} \quad . \tag{17}$$

3.2 ASTREX Model: Design Assumptions

The NASTRAN analysis of the ASTREX model supplies the matrices Ω and Φ described in the previous section.

There are 30 modes ranging from 12.25 Hz to 71.03 Hz (see Table 2) .

There is a 4 Hz mode due to pedestal motion which has been neglected for this study. A uniform damping ratio of $\zeta = 0.002$ is assigned to each mode to obtain the state-matrix A as in (16). The following input-output description and actuator/sensor assignment is assumed to build up the ASTREX model used in controller design (see Figure 16 for the node locations):

- The input matrix $B_{\mathrm{sec}} \in \mathrm{I\!R}^{60 \times 2}$ corresponds to secondary-mirror proof-mass actuators at node 100; these x- and y-directional actuators are assumed to have a maximum thrust of 8.9 N [1] .

- The input matrix $B_{\mathrm{pri}} \in \mathrm{I\!R}^{60 \times 18}$ corresponds to the primary-mirror x- , y- and z-directional thruster inputs at nodes 1 , 4 , 31 , 37 , 64 and 67; these thrusters are for station-keeping and slewing maneuvers; they have a maximum thrust of 890 N . During slewing about the x- and y-axes, the four z-directional thrusters at nodes 1 , 4 , 64 and 67 are used; the input matrix B_{slew} consists of the columns of B_{pri} corresponding to the z-directional thrusters at nodes 1 , 4 , 64 and 67 .

Table 2: The 30 modes of the ASTREX model (excluding the 4 Hz pedestal mode)

mode no.	modal frequency (Hz)
1	12.25
2	12.59
3	14.65
4	17.80
5	22.14
6	25.09
7	25.38
8	29.01
9	29.96
10	30.10
11	30.70
12	32.08
13	35.16
14	35.54
15	36.59
16	38.56
17	43.97
18	44.75
19	48.60
20	49.19
21	49.49
22	52.27
23	53.00
24	56.23
25	57.36
26	63.17
27	65.09
28	66.95
29	68.60
30	71.03

- The output matrix $C_{\text{los}} \in \mathbb{R}^{2 \times 60}$ determines the line-of-sight (LOS) deflection about the x- and y-axes; LOS consists of predetermined rotations and translations of the three mirrors in Figure 16 .

- There are colocated (rate-damping) actuators and sensors at nodes 1 , 4 , 31 , 37 , 64 , 67 and 100 . Hence $B_{\text{pri}}{}^T$ is the output matrix which determines the velocities at the primary mirror nodes 1 , 4 , 31 , 37 , 64 and 67 . Similarly, $B_{\text{sec}}{}^T$ determines the velocities at node 100 .

From the input-output description mentioned above, we obtain the following plant transfer matrix:[6]

$$
P = \left[
\begin{array}{cc}
A & \left[\begin{array}{ccc} B_{\text{sec}} & B_{\text{slew}} & B_{\text{pri}} \end{array}\right] \\
\left[\begin{array}{c} C_{\text{los}} \\ B_{\text{sec}}^T \\ B_{\text{pri}}^T \end{array}\right] & 0
\end{array}
\right] . \tag{18}
$$

---

[6]The notation $G = \left[\begin{array}{cc} A & B \\ C & D \end{array}\right]$ is used as a shorthand to denote the transfer matrix

$G = C(sI - A)^{-1}B + D$.
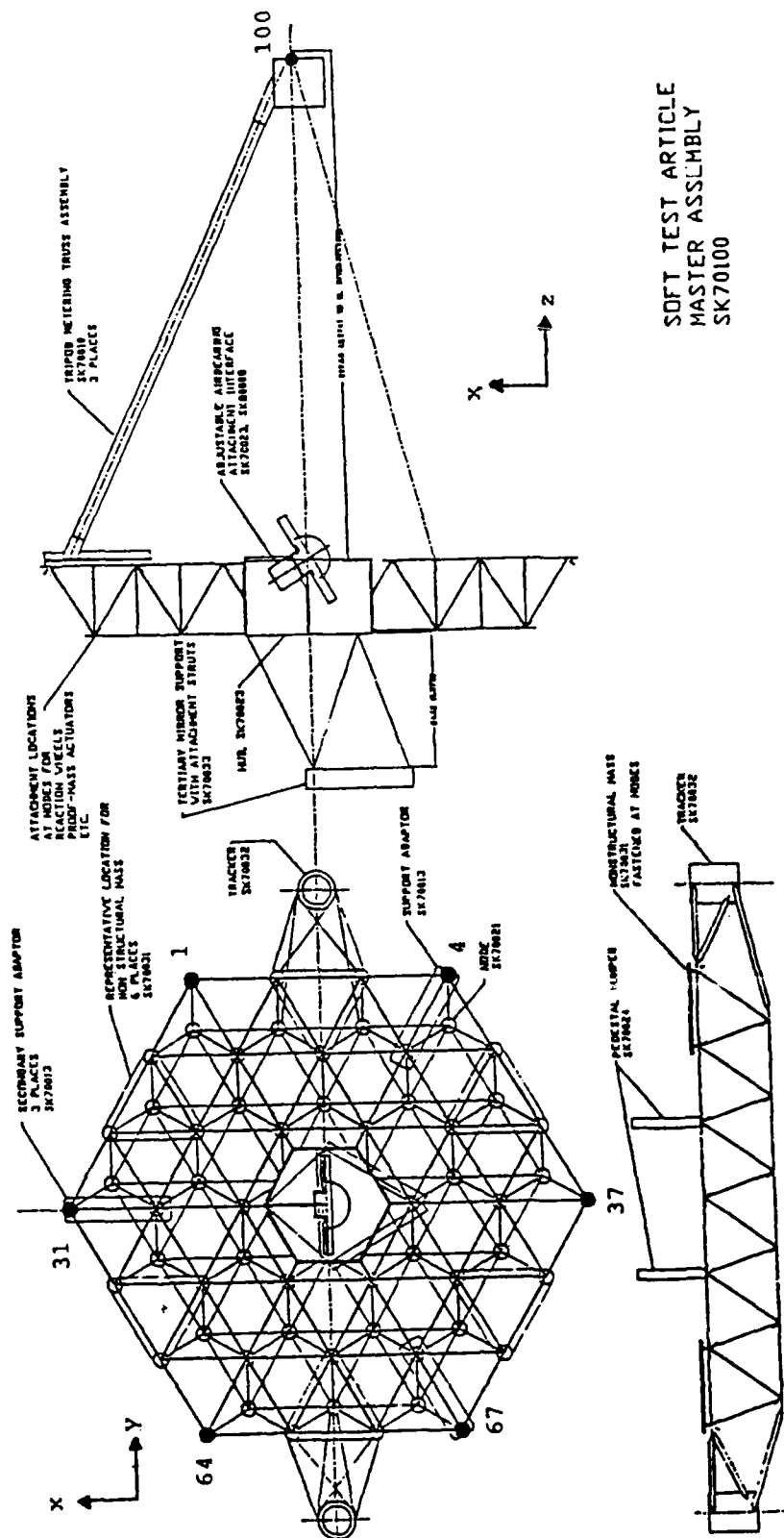
Figure 16: Drawing of the test article indicating nodes 1, 4, 31, 37, 64, 67 and 100 (Boeing Aerospace)

4 Low-Authority Control Design

Consider the ASTREX model in (18), where the primary mirror actuators and sensors are colocated. Let the transfer function from the primary mirror actuators to the primary mirror sensors be denoted by $P_{y_{\mathrm{pri}}u_{\mathrm{pri}}}$; from (16),(17) and (18), we obtain

$$
\begin{aligned}
P_{y_{\mathrm{pri}}u_{\mathrm{pri}}} &= B_{\mathrm{pri}}{}^T(sI - A)^{-1}B_{\mathrm{pri}} \\
&= \sum_{k=1}^{30} \frac{s}{s^2 + 0.004\omega_k s + \omega_k^2} b_k b_k^T \quad,
\end{aligned}
\tag{19}
$$

where b_k^T denotes the $(30 + k)$th row of B_{pri} . Since $b_k b_k^T$ is positive semi-definite [7] for $k = 1, \ldots, 30$, the transfer function $P_{y_{\mathrm{pri}}u_{\mathrm{pri}}}$ in (19) is passive. [8] Hence, if we choose

$$
u_{\mathrm{pri}} = -K y_{\mathrm{pri}} \quad,
\tag{20}
$$

where the matrix K is positive-definite, [9] then the closed-loop system is stable. In fact, stability is guaranteed if the matrix K in (20) is replaced by *any* transfer function which is strictly-passive. [10] Note that a positive-definite matrix K is strictly-passive. Since a well-posed interconnection of a strictly-passive linear subsystem and a passive linear subsystem in the standard unity-feedback configuration is exponentially stable, *any* control law in the form of (20) will *not* destabilize the plant [7] .

Now choose the rate-feedback matrix in (20) as

$$
K = k_{\mathrm{lac}}I \quad,
$$

where k_{lac} denotes the rate-feedback gain and I denotes the identity-matrix (in this case, 18 by 18). Colocated velocity-feedback is applied at the primary mirror nodes 1 , 4 , 31 , 37 , 64 and 67 in order to increase the damping ratios of A in (18). Let

$$
A_{\mathrm{lac}} := A - k_{\mathrm{lac}}B_{\mathrm{pri}}B_{\mathrm{pri}}^T \quad.
$$

After the low-authority control is applied at the primary mirror colocated actuators and sensors, we obtain the plant description P_{lac} (see Figure 17; d_{sec} denotes the disturbance at the secondary mirror):

$$
P_{\mathrm{lac}} := \left[\begin{array}{c|cc} A_{\mathrm{lac}} & B_{\mathrm{sec}} & B_{\mathrm{slew}} \\ \hline \begin{bmatrix} C_{\mathrm{los}} \\ B_{\mathrm{sec}}^T \end{bmatrix} & & 0 \end{array} \right] \quad.
\tag{21}
$$

---

[7] A symmetric matrix Q is said to be positive semi-definite iff $x^T Q x \geq 0$ for all x .

[8] A transfer matrix P is said to be passive iff the symmetric matrix $[P(j\omega) + (P(j\omega))^*]$ is positive semi-definite for all real ω .

[9] A symmetric matrix Q is said to be positive-definite iff $x^T Q x > 0$ for all $x \neq 0$.

[10] A transfer matrix Q is said to be strictly-passive iff there exists a δ positive such that $\lambda_{\min}[(Q(j\omega) + (Q(j\omega))^*] \geq \delta > 0$ for all real ω .
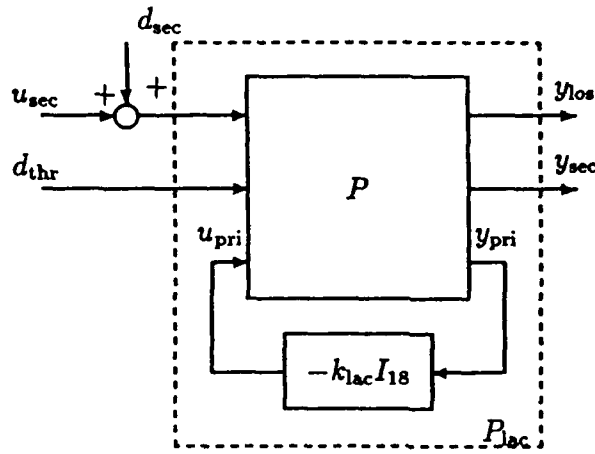
Figure 17: The plant model before (P) and after LAC (P_{lac})

For $k_{\text{lac}} = 7000$, the damping ratios of A_{lac} are shown in Figure 18 ; the maximum damping ratio is approximately 0.04 .
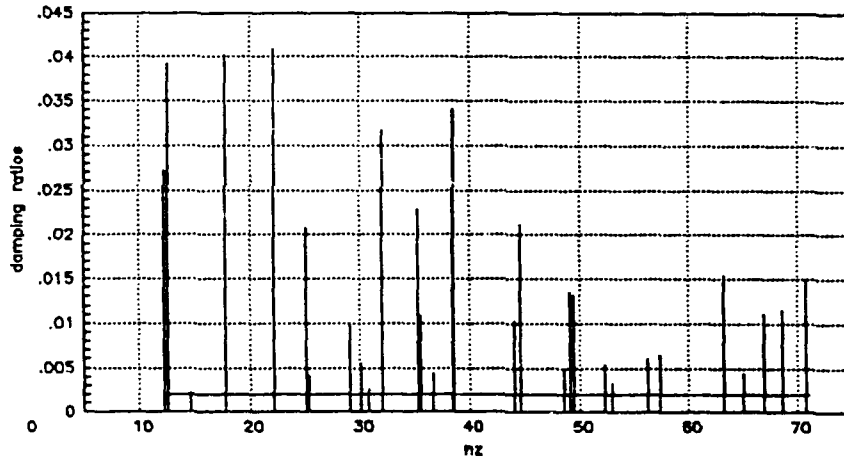
Figure 18: Damping ratios for the 30 modes before (a horizontal line at $\zeta = 0.002$ is drawn for reference) and after colocated rate-feedback at the primary mirror nodes

Let $P_{y_{\text{los}} u_{\text{sec}}}$ and $P_{\text{lac}, y_{\text{los}} u_{\text{sec}}}$ denote the transfer functions $u_{\text{sec}} \mapsto y_{\text{los}}$ before and after colocated velocity-feedback at the primary mirror nodes, respectively; then, we obtain

$$P_{y_{\text{los}} u_{\text{sec}}} = C_{\text{los}} (sI - A)^{-1} B_{\text{sec}} \tag{22}$$

$$P_{\text{lac}, y_{\text{los}} u_{\text{sec}}} = C_{\text{los}} (sI - A_{\text{lac}})^{-1} B_{\text{sec}} \quad . \tag{23}$$

The state matrix A in (18) has lightly-damped modes by construction (see (16)). After colocated velocity feedback at the primary mirror nodes, $\det(sI - A_{\text{lac}})$ is still

30

strictly Hurwitz for reasons explained above. Hence $P_{y_{los}u_{sec}}$ and $P_{lac,y_{los}u_{sec}}$ defined above are stable transfer matrices. The maximum singular-value plots[11] of $P_{y_{los}u_{sec}}$ and $P_{lac,y_{los}u_{sec}}$ are shown in Figures 19 and 20 , respectively. Due to LAC, the increase in the damping ratios has smoothed out the peaks.
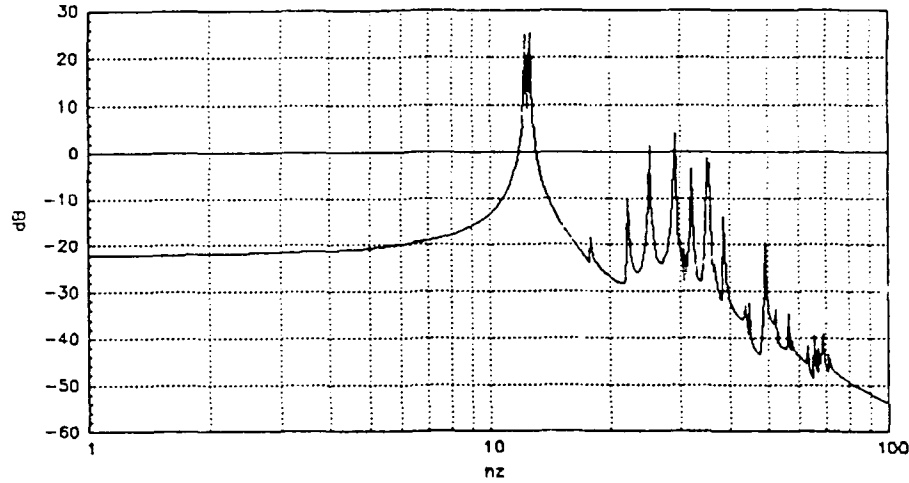
Figure 19: $20\log(\bar{\sigma}(P_{y_{los}u_{sec}}(j\omega)))$ $[\mu rad/N]$: Singular-value plot of the (openloop) transfer function from the secondary mirror actuators to the line-of-sight
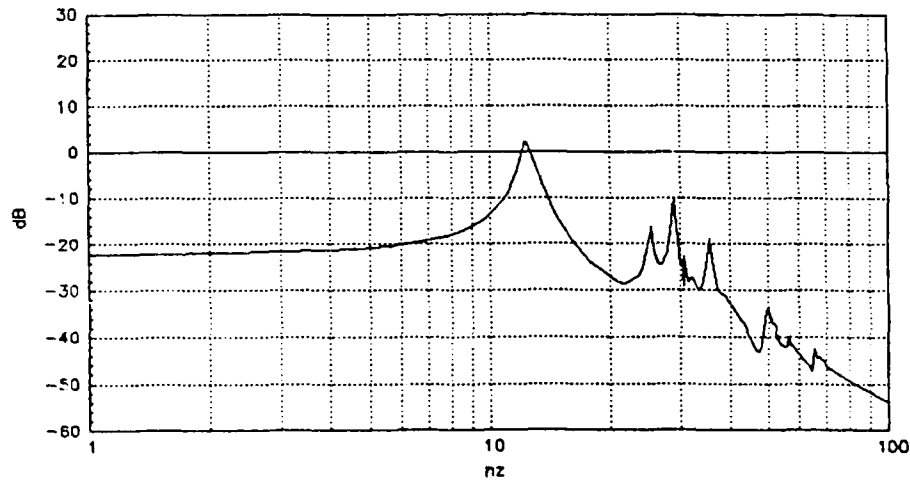
Figure 20: $20\log(\bar{\sigma}(P_{lac,y_{los}u_{sec}}(j\omega)))$ $[\mu rad/N]$: Singular-value plot of the (closed-loop) transfer function from the secondary mirror actuators to the line-of-sight after LAC

---

[11]For a given complex matrix (not necessarily square) H , let $\bar{\sigma}(H)$ denote the maximum eigenvalue of H^*H ($*$ denotes the complex conjugate transpose). For a *stable* transfer matrix H, the maximum singular-value plot of H is the graph $(\omega, \bar{\sigma}(H(j\omega)))$ $\omega \geq 0$.

31

4.1 Limitations of Rate Feedback

Consider the plant description in (18) (no low-authority control applied), where the diagonal matrix Ω (in A, see (16)) is positive-definite. Due to the structure of the state-matrix (16) and input-matrices (17), for any rate-feedback law (not necessarily stabilizing, utilizing all possible rate measurements at the primary and secondary mirror colocated actuator and sensors) of the form

$$\begin{bmatrix} u_{\text{sec}} \\ u_{\text{pri}} \end{bmatrix} = K \begin{bmatrix} y_{\text{sec}} \\ y_{\text{pri}} \end{bmatrix} , \tag{24}$$

where K is any real matrix, the closed-loop map from d_{sec} to y_{los} has a blocking-zero at $s=0$, i.e., the transfer function is identically zero at $s=0$. This structure dependent result is due to the following straightforward calculation:

$$\begin{bmatrix} 0 & \widehat{C}_2 \end{bmatrix} \begin{bmatrix} sI & -I \\ \Omega^2 & sI+M \end{bmatrix}^{-1} \begin{bmatrix} 0 \\ \widehat{B} \end{bmatrix} = s\,\widehat{C}_2 \left(s^2 I + Ms + \Omega^2\right)^{-1} \widehat{B} ,$$

where M denotes any $n \times n$ matrix; $\widehat{C}_2$ and $\widehat{B}^T$ have at most n columns.

A similar calculation shows that

$$\begin{bmatrix} \widehat{C}_1 & 0 \end{bmatrix} \begin{bmatrix} sI & -I \\ \Omega^2 & sI+M \end{bmatrix}^{-1} \begin{bmatrix} 0 \\ \widehat{B} \end{bmatrix} = \widehat{C}_1 \left(s^2 I + Ms + \Omega^2\right)^{-1} \widehat{B} ,$$

where M denotes any $n \times n$ matrix; $\widehat{C}_1$ and $\widehat{B}^T$ have at most n columns. Hence, regardless of the rate-feedback chosen (which will only affect the matrix M), the closed-loop transfer function $H_{y_{\text{los}}d_{\text{sec}}}$ (after the feedback law in (24) is applied to the plant in (18)) from d_{sec} to y_{los} satisfies

$$H_{y_{\text{los}}d_{\text{sec}}}(0) = C_{\text{los}}(sI - A + [B_{\text{sec}} \;\; B_{\text{pri}}]K \begin{bmatrix} B_{\text{sec}}^T \\ B_{\text{pri}}^T \end{bmatrix})^{-1}\Big|_{s=0} B_{\text{sec}} = \widehat{C}_{\text{los}}\Omega^{-2}\widehat{B}_{\text{sec}} .$$

where $\widehat{C}_{\text{los}}$ denotes the first 30 columns of C_{los} and $\widehat{B}_{\text{sec}}$ denotes the last 30 rows of B_{sec}.

If constant rate-feedback (as in (24)) does not affect $H_{y_{\text{los}}d_{\text{sec}}}(0)$, can it be changed by dynamic output-feedback from y_{sec} to u_{sec}? The answer is negative due to the blocking zero at $s=0$, as explained above. Let C denote the transfer function of the stabilizing output feedback compensator from y_{sec} to u_{sec}. The achievable closed-loop transfer function from d_{sec} to y_{los} is given by

$$H_{y_{\text{los}}d_{\text{sec}}} := P_{y_{\text{los}}u_{\text{sec}}} \left(I + C P_{y_{\text{sec}}u_{\text{sec}}}\right)^{-1} ;$$

since $P_{y_{\text{sec}}u_{\text{sec}}}(0) = 0$, for all stabilizing compensators

$$H_{y_{\text{los}}d_{\text{sec}}}(0) = P_{y_{\text{los}}u_{\text{sec}}}(0) = \widehat{C}_{\text{los}}\Omega^{-2}\widehat{B}_{\text{sec}} .$$

In other words, any LAC and HAC combination using rate-feedback alone (no displacement feedback) will not affect the DC-gain of the map from d_{sec} to y_{los}.

5 HAC : No LOS Measurements

5.1 Disturbance Modeling

Consider the plant model P_{lac} in (21) obtained by applying LAC to P in (18) at the primary mirror nodes (see Figure 17) . There are three sources of disturbances that are considered in the design (see Figure 21):

- The disturbance d_{sec} comes in additively at the secondary mirror actuator inputs (e.g., disturbances due to coolant flow); d_{sec} is assumed to be of the form

$$d_{sec} = \frac{s}{s + 4\pi} I d \quad ,$$

where d denotes any bounded disturbance.

- The output disturbance d_{out} denotes the wide-band sensor noise at the secondary mirror velocity measurements.

- The third disturbance d_{thr} is a low-frequency disturbance (up to 2 Hz) due to the z-directional thruster inputs during slewing about the x- and y-axes.

The objective is to design an output feedback compensator at the proof-mass actuators at node 100 such that the secondary mirror disturbance d_{sec} is attenuated at the line-of-sight y_{los} ; the design will also take into account the affect of the low-frequency slewing command d_{thr} at the line-of-sight.
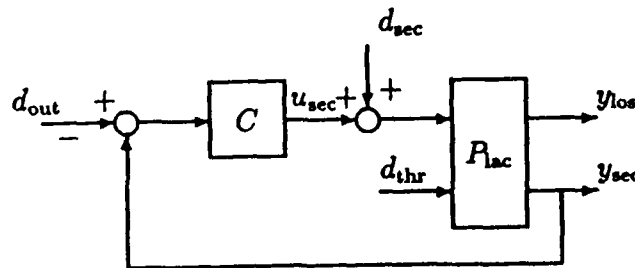
Figure 21: High-authority rate-feedback controller C at node 100

5.2 Model Reduction

Before proceeding with the high-authority control (HAC) design, which will provide high damping to meet the performance requirements, a reduced-order version of the 60-state plant in (21) is obtained.

One way of determining "important" modes, i.e., those modes that will be kept in the reduced-order model, is to do a balancing transformation to determine a modal ranking which reflects the "importance" of each mode in terms of joint controllability and observability [29].

An asymptotically stable state-space description

$$
\begin{aligned}
\dot{x} &= A_{bal}x + B_{bal}u \\
y &= C_{bal}x
\end{aligned}
$$

is said to be *internally balanced* iff

$$
\begin{aligned}
\int_0^\infty e^{A_{bal}t}B_{bal}B_{bal}^T e^{A_{bal}^T t}dt &= \int_0^\infty e^{A_{bal}^T t}C_{bal}^T C_{bal}e^{A_{bal}t}dt \\
&= \text{diag}[\sigma_1^2,\ldots,\sigma_n^2] \ , \sigma_i^2 \geq \sigma_j^2 \ , i \geq j \ \ .
\end{aligned}
$$

Each of the states (x_i) in the internally balanced state-space description corresponds to one the singular-values (σ_i^2) . A relatively small singular-value implies that the corresponding state is weakly controllable and weakly observable (i.e., too much gain is required to control and estimate that state) . If the original state-description is not internally balanced, the required state transformation (which puts the state-space description into an internally balanced form) "scrambles" the original coordinate system and the physical meaning of the original states is lost.

For the plant description in (21) , the following steps are taken to obtain the modal rankings shown in Figures 22 and 23 :

1. Each of the state-space descriptions $(B_{sec}{}^T, A_{lac}, B_{sec})$ and $(C_{los}, A_{lac}, B_{sec})$ are transformed into balanced realizations.

2. Approximating each mode ω_i in the balanced coordinates as the square-root of the determinant of the thirty two-by-two diagonal subblocks in the respective transformed state matrices, the modal rankings of the thirty modes are obtained.

34
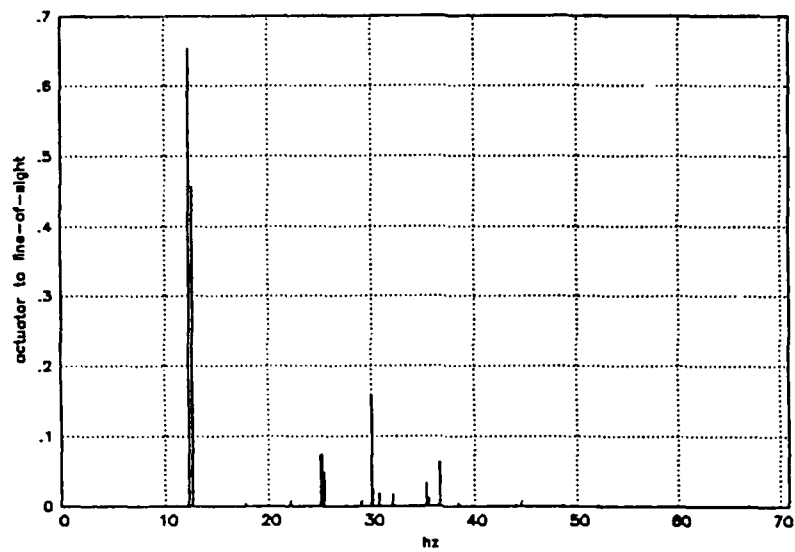
Figure 22: Modal ranking ($1E6 * \sigma_i^2$, $i = 1, \ldots, 30$) for the actuator to line-of-sight map in (21)
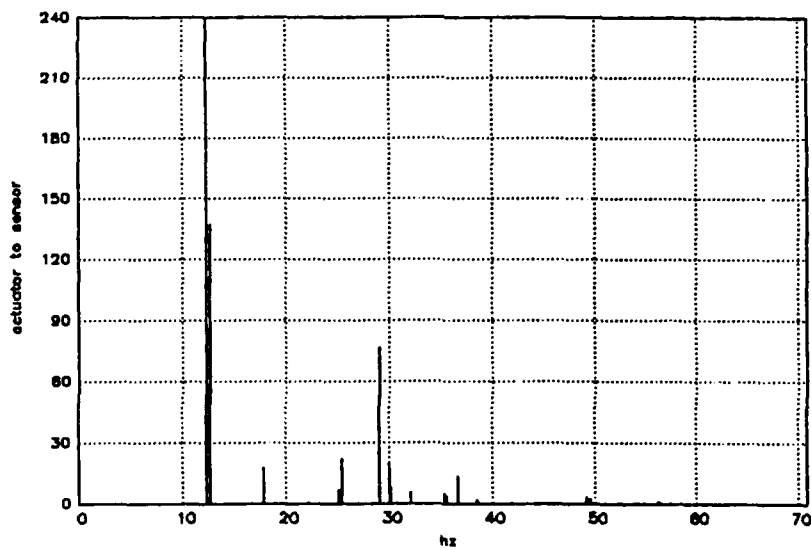
Figure 23: Modal ranking ($1E6 * \sigma_i^2$, $i = 1, \ldots, 30$) for the actuator to sensor map in (21)

Instead of just proceeding with a modal reduction based on the modal rankings in Figures 22 and 23 (i.e., deleting modes ω_i with "small" σ_i^2), we also checked the relative-error introduced by the reduced-order model when compared with the 60-state model in (21) ; here we follow the procedure in [30].

Let $P_{\text{lac},y_{sec}u_{sec}}$ and $\tilde{P}_{\text{lac},y_{sec}u_{sec}}$ denote the transfer functions from u_{sec} to y_{sec} for the 60-state model in (21) and its reduced-order model, respectively. Suppose that we represent $P_{\text{lac},y_{sec}u_{sec}}$ as a perturbation (post-multiplicative) of $\tilde{P}_{\text{lac},y_{sec}u_{sec}}$, where

$$P_{\text{lac},y_{sec}u_{sec}} = (I + \Delta)\tilde{P}_{\text{lac},y_{sec}u_{sec}} \tag{25}$$

for some *stable* Δ . Let us ask the following question: under which conditions can we guarantee that a compensator that stabilizes $\tilde{P}_{\text{lac},y_{sec}u_{sec}}$ also stabilizes $P_{\text{lac},y_{sec}u_{sec}}$? One conservative answer to this general question can be given by a small-gain argument using singular-values.

Suppose that a proper compensator C (not necessarily stable) stabilizes $\tilde{P}_{\text{lac},y_{sec}u_{sec}}$ (in the standard unity-feedback configuration); hence the closed-loop map

$$H := C\tilde{P}_{\text{lac},y_{sec}u_{sec}}(I + C\tilde{P}_{\text{lac},y_{sec}u_{sec}})^{-1}$$

is proper and stable.

Since the perturbation Δ is proper and stable, the compensator C stabilizes $P_{\text{lac},y_{sec}u_{sec}}$ *if and only if* the stable transfer matrix $(I + \Delta H)$ has a stable inverse. The condition

$$\bar{\sigma}((\Delta H)(j\omega)) < 1 \quad \forall \omega \in \mathbb{R} \quad ,$$

or more conservatively,

$$\bar{\sigma}(\Delta(j\omega))\bar{\sigma}(H(j\omega)) < 1 \quad \forall \omega \in \mathbb{R} \quad ,$$

guarantees that the map $(I + \Delta H)$ *has* a stable inverse.

In our case, $P_{\text{lac},y_{sec}u_{sec}}$ in (25) is square; solving for Δ , we obtain the relative error

$$\bar{\sigma}(\Delta(j\omega)) = \bar{\sigma}((P_{\text{lac},y_{sec}u_{sec}}\tilde{P}_{\text{lac},y_{sec}u_{sec}}^{-1})(j\omega) - I) \quad .$$

If $\bar{\sigma}(\Delta(j\omega)) \leq 1$ (determined during model reduction) and if $\bar{\sigma}(H(j\omega)) < 1$ (determined during HAC design), one can guarantee that the HAC design withstands the specific perturbation Δ . In case these conditions fail, nothing can be said until the final closed-loop eigenvalues are checked.

Along this line of thinking, the first thirteen modes (since the band of interest is up to 30 Hz range) were kept and the relative-error plot was checked. The third and the fourth modes (weakly disturbable and observable (see Figure 22)) were dropped since they did not change the relative-error plot significantly. Hence, the 22-state version of the plant in (21) was obtained by modal truncation, keeping modes 1 , 2 , 5 -- 13 ; the associated relative error is shown in Figure 24.

36
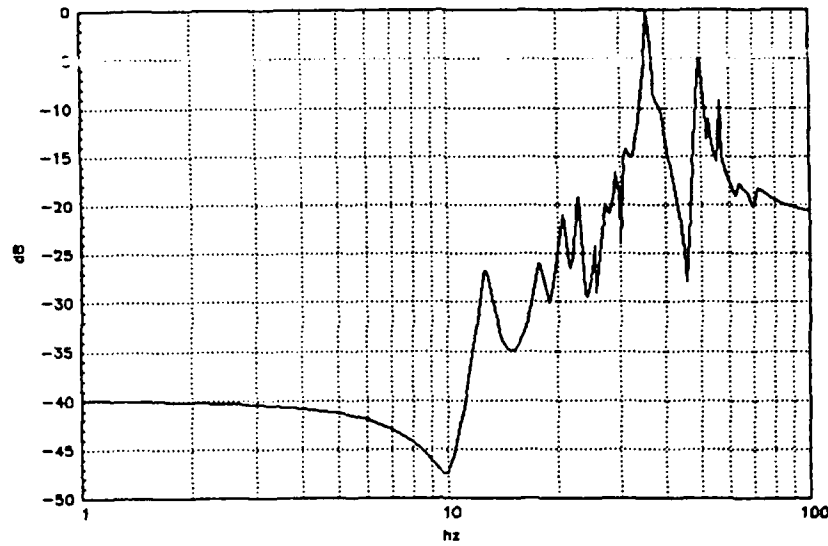
Figure 24: Relative error for the 22-state plant, $20 \log(\bar{\sigma}(\Delta(j\omega)))$ (see (25))

For high-authority control (HAC) design, the 22-state model $\tilde{P}_{lac}$ is used ((26) in $MATRIX_X$ notation).

$$index := [1\,2\,5:13\,31\,32\,35:43]$$

$$\tilde{P}_{lac} := \left[\begin{array}{cc} A_{lac}(index,index) & B_{sec}(index,:) \;\; B_{slew}(index,:) \\ \left[\begin{array}{c} C_{los}(:,index) \\ (B_{sec}(index,:))^T \end{array} \right] & 0 \end{array} \right] . \quad (26)$$

5.3   High-Authority Control Design

The $\mathcal{H}_\infty$-design methodology is used to design a dynamic output-feedback compensator from y_{sec} to u_{sec} for the 22-state plant $\tilde{P}_{lac}$ in (26) . A brief outline of this methodology is given below.

5.3.1 $\mathcal{H}_\infty$-Design

Consider the two-vector-input two-vector-output plant $\tilde{P}_{aug}$ shown in Figure 25.

The input d denotes the disturbances acting on the model; z denotes the regulated variables; u and y denote the control inputs and measured outputs used in feedback, respectively. For a linear time-invariant finite-dimensional (not necessarily stable) plant $\tilde{P}_{aug}$ as in Figure 25 , the set of all stabilizing compensators C (not necessarily stable) such that the closed-loop system in Figure 26 is stable can be parametrized.

37
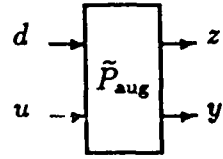
Figure 25: Two-input two-output plant $\tilde{P}_{\text{aug}}$
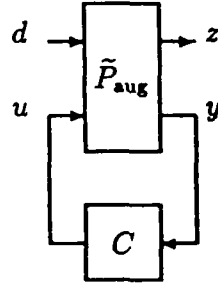
Figure 26: Stable closed-loop system

The plant $\tilde{P}_{\text{aug}}$ is assumed to satisfy a necessary condition for stabilizability: all of the "instabilities" in $\tilde{P}_{\text{aug}}$ must be seen in the map from u to y. An intuitive explanation can be made as follows: if there are any instabilities in the map from d to z which do not show up in the map from u to y nothing can be done about these instabilities by closing the loop from y to u.

The $\mathcal{H}_\infty$-design method solves the following problem:

Given $\tilde{P}_{\text{aug}}$ and $\gamma > 0$, find a compensator C such that the closed-loop system in Figure 26 is stable and

$$\sup_\omega \bar{\sigma}(H_{zd}(j\omega)) < \gamma ; \qquad (27)$$

H_{zd} denotes the stable closed-loop map from d to z in Figure 26.

Note that the inequality in (27) allows the designer to do frequency-shaping at the regulated variables. Suppose that in our case we set

$$z_1 = W_{\text{los}} y_{\text{los}} , \qquad (28)$$
$$d_1 = d_{\text{sec}} , \qquad (29)$$

where the *scalar* transfer function W_{los} is chosen such that it is stable and has a proper stable inverse. From (27), (28) and (29), we obtain

38

$$\gamma > \bar{\sigma}(H_{zd}(j\omega)) \geq \bar{\sigma}(H_{z_1 d_1}(j\omega))$$
$$= \bar{\sigma}((W_{\text{los}} H_{y_{\text{los}} d_{\text{sec}}})(j\omega))$$
$$= |W_{\text{los}}(j\omega)| \, \bar{\sigma}(H_{y_{\text{los}} d_{\text{sec}}}(j\omega)) \quad ;$$

hence

$$\bar{\sigma}(H_{y_{\text{los}} d_{\text{sec}}}(j\omega)) < \gamma \, |W_{\text{los}}(j\omega)|^{-1} \quad .$$

In other words, by choosing the weight W_{los} such that $\gamma |W_{\text{los}}(j\omega)|^{-1}$ is below the specifications, the closed-loop map $H_{y_{\text{los}} d_{\text{sec}}}$ of interest meets the desired disturbance to line-of-sight specifications.

In the next subsection, we explain how the augmented plant $\tilde{P}_{\text{aug}}$ is obtained.

5.3.2 Augmented Reduced-Order Plant $\tilde{P}_{\text{aug}}$

From $\tilde{P}_{\text{lac}}$ in (26), we construct the augmented plant $\tilde{P}_{\text{aug}}$ with weights $W_1, \ldots, W_5$ as shown in in Figure 27 .
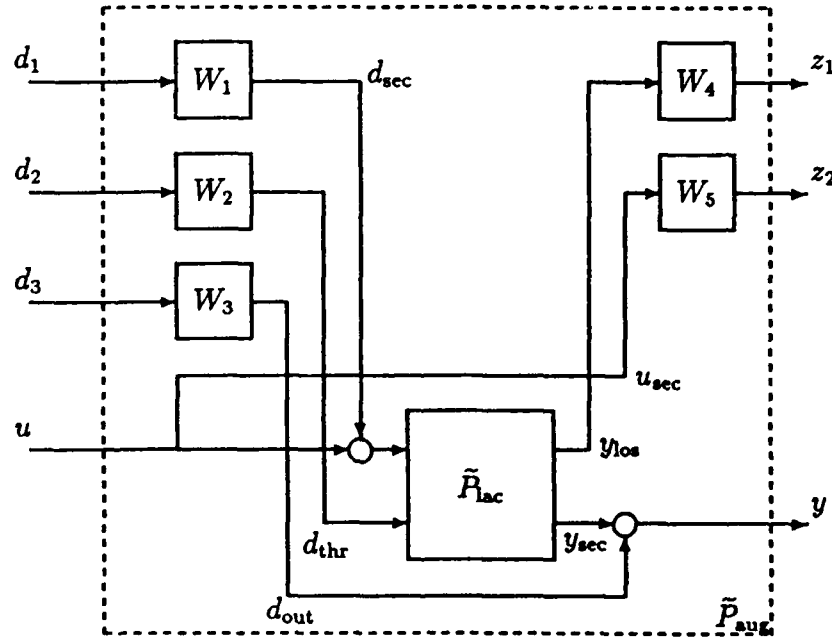
Figure 27: $\tilde{P}_{\text{aug}}$ obtained by augmenting the 22-state reduced plant $\tilde{P}_{\text{lac}}$

The weights $W_1, \ldots, W_5$ are chosen as follows:

W_1 : high-pass with cutoff at 2 Hz ($W_1 = \frac{s}{s+4\pi} I_2$). The secondary mirror actuator disturbance d_{sec} is assumed to be isolated from the low-frequency (up to 1 Hz) disturbance due to the z-directional thrusters.

39

W_2 : lowpass with cut-off at 1 Hz ($W_2 = \frac{2\pi}{s+2\pi} I_4$). The z-directional thruster inputs during slewing is assumed to be band-limited up to 1 Hz .

W_3 : wideband noise at the sensor outputs ($W_3 = 0.1 I_2$).

W_4 : bandpass with poles at 5 Hz , zeros at 2 Hz ($W_4 = 62.5 \frac{(s+4\pi)^2}{(s+10\pi)^2} I_2$). The inverse of this weight is the line-of-sight spec.

W_5 : actuator weight; chosen to have less actuator authority up to 1 Hz in order to limit $d_{\text{thr}} \mapsto u_{\text{sec}}$ during slewing ($W_5 = \frac{s+20\pi}{s+2\pi} I_2$).

The weights $W_1, \ldots, W_5$ are the design "knobs". Not all settings are feasible; i.e., for certain choices of weights, there may not be any compensator that meets the specifications. It is up to the designer to set these weights accordingly, so that the desired performance can be achieved by dynamic compensation.

Using $\tilde{P}_{\text{aug}}$ in Figure 25 and the state-space solution to $\mathcal{H}_\infty$-controller design [8] , a 34-state compensator is designed. The closed-loop system satisfies

$$\sup_\omega \bar{\sigma}(H_{zd}(j\omega)) < 2 \quad,$$

hence the line-of-sight spec (the inverse of the line-of-sight weight W_4) is met within at most 6 dB .

The 34-state compensator obtained by the $\mathcal{H}_\infty$-design stabilizes the 60-state plant in (21) (verified by checking the closed-loop eigenvalues).

5.4   Closed-Loop Performance

In this section, we present the performance data for the stable closed-loop system in Figure 21 ; C denotes the 34-state compensator obtained by $\mathcal{H}_\infty$-design and P_{lac} denotes the 60-state plant model with low-authority control applied at the primary-mirror nodes (see (21) , Figure 17) .

The maximum singular-value plots of the six transfer matrices (from (d_{sec} , d_{out} , d_{thr}) to (y_{los} , y_{sec})) of the closed-loop system in Figure 21 are shown in Figures 28 and 29 .
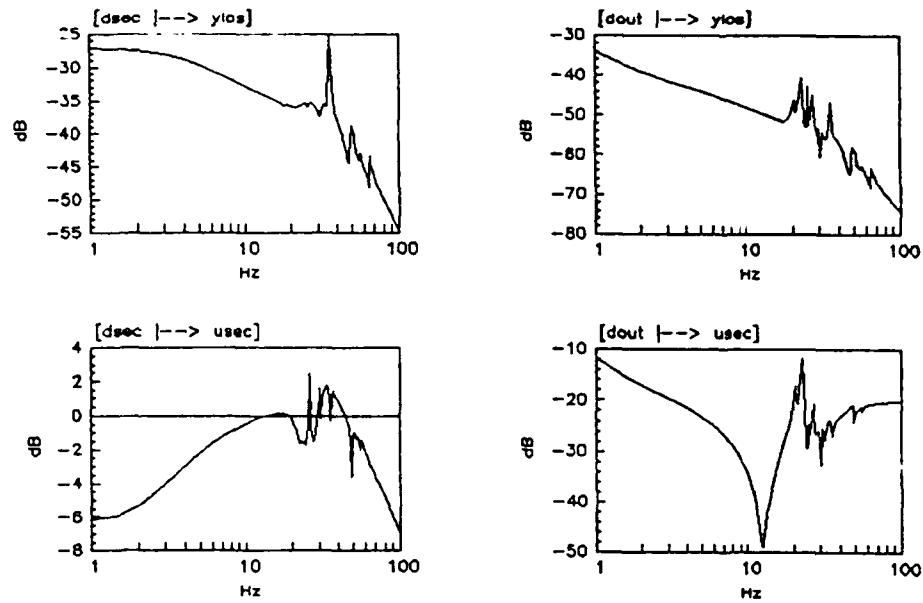
Figure 28:

Singular-value plots of the four transfer matrices $d_{sec} \mapsto y_{los}$, $d_{sec} \mapsto u_{sec}$, $d_{out} \mapsto y_{los}$ and $d_{out} \mapsto u_{sec}$ of the closed-loop (LAC/HAC) system in Figure 21 .
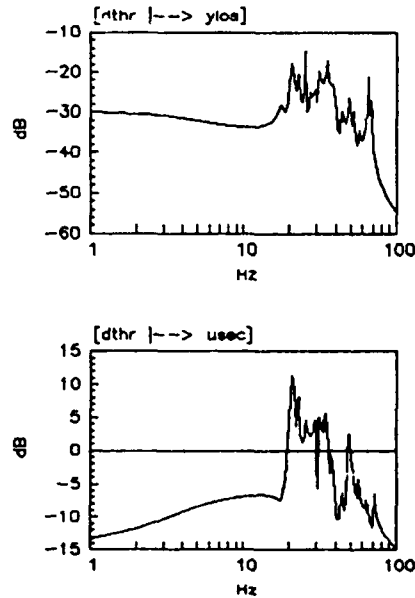
Figure 29:

Singular-value plots of the two transfer matrices $d_{thr} \mapsto y_{los}$ and $d_{thr} \mapsto u_{sec}$ of the closed-loop (LAC/HAC) system in Figure 21 .

41

5.4.1 Disturbance Attenuation at the Line-of-Sight

Let the closed-loop transfer function (after LAC and HAC) from d_{sec} to y_{los} in Figure 21 be denoted by $H_{y_{los}d_{sec}}$. The maximum singular-value plot of $H_{y_{los}d_{sec}}$ is shown in Figure 30 .
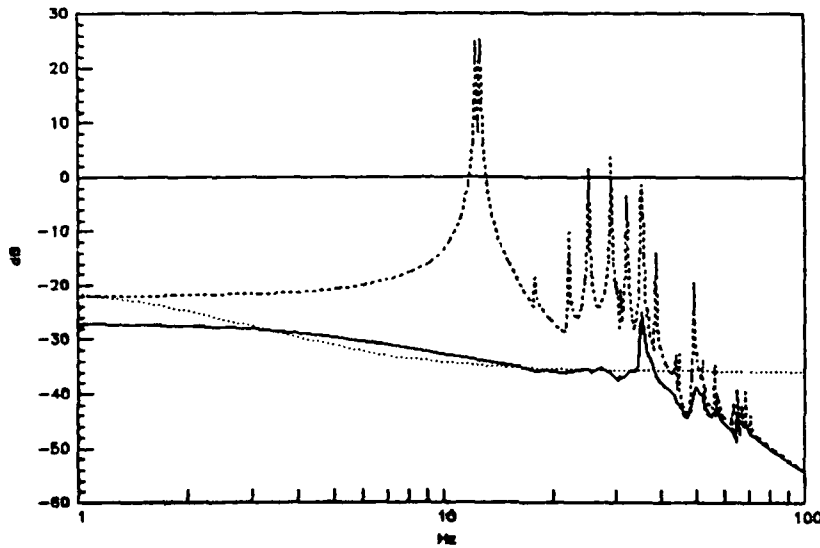
Figure 30:

- - - $\bar{\sigma}(C_{los}(j\omega I - A)^{-1}B_{sec})$ $[\mu rad/N]$: open-loop d_{sec} to y_{los} before LAC

.... $-20\log(|W_4(j\omega)|)$: magnitude plot of the inverse of the line-of-sight weight W_4 (i.e., the line-of-sight spec) in Figure 27 .

—— $\bar{\sigma}(H_{y_{los}d_{sec}}(j\omega))$ $[\mu rad/N]$: closed-loop (after LAC and HAC, see Figure 21) d_{sec} to y_{los}

The following subsections evaluate the line-of-sight performance with different measures.

42

5.4.2 $\mathcal{H}_\infty$-norm

For a given stable transfer matrix H the $\mathcal{H}_\infty$-norm of H is defined by

$$\|H\|_\infty := \sup_{\omega \in [0,\infty)} \bar{\sigma}\left(H(j\omega)\right) \; ;$$

that is

$$\bar{\sigma}\left(H(j\omega)\right) \leq \|H\|_\infty \quad \text{for all} \quad \omega \in \mathbb{R} \; .$$

The $\mathcal{H}_\infty$-norm is an induced-norm (i.e., the "gain" associated with a stable transfer matrix) over the set of signals with bounded energies [12]. In other words, the following inequality holds:

$$\|Hu\|_2 \leq \|H\|_\infty \|u\|_2 \; .$$

If a signal u of unit energy is applied to the stable system with transfer matrix H the output energy can be at most $\|H\|_\infty^2$ units; hence $\|H\|_\infty^2$ is the worst case energy gain. In fact, there does exit a signal with unit energy which achieves an output with the worst case energy.

The singular-value plot of the open-loop map from u_{sec} to y_{los} (for the description in (18)), peaks to 26 dB around 10 Hz (see Figure 30). A worst case disturbance around 10 Hz with one unit energy will yield an output with 19.95 units of energy. The final closed-loop (after LAC/HAC) map from d_{sec} to y_{los} in Figure 21 achieves its maximum singular-value at 0 Hz (out of the range of Figure 30, however as explained in the previous section nothing can be done about this value as long as only rate-feedback is used). However, over the band 2 Hz – 30 Hz , the square of the $\mathcal{H}_\infty$-norm (namely, the energy gain) has been reduced by 52 dB from 26 dB .

5.4.3 $\mathcal{H}_2$-norm

For a strictly proper stable transfer matrix H , where

$$H(s) := C\left(sI - A\right)^{-1}B \; ,$$

the $\mathcal{H}_2$-norm , $\|H\|_2$, of H is defined as

$$
\begin{aligned}
\|H\|_2 &:= \left(\text{trace}(B^T W_o B)\right)^{1/2} \\
&= \left(\text{trace}(C W_c C^T)\right)^{1/2} \\
&= \left(\frac{1}{2\pi} \int_{-\infty}^{\infty} \text{trace}(H(j\omega)(H(j\omega))^*)d\omega\right)^{1/2} \; ;
\end{aligned}
$$

the trace of a square matrix denotes the sum of the diagonal entries; W_c and W_o denote the controllability and observability gramians of the triple (C, A, B) ; equivalently, they

---

[12](a one-sided signal u (i.e., $u(t)$ is zero for t negative) is said to have bounded energy iff $\|u\|_2^2 < \infty$, where $\|u\|_2^2 := \int_0^\infty |u(t)|^2 dt$).

are the solutions to the following set of linear equations:

$$AW_c + W_cA^T = -BB^T$$
$$A^TW_o + W_oA = -C^TC \quad .$$

One word of caution is that $\mathcal{H}_2$-norm is not an induced norm; given two stable transfer matrices H_1 and H_2,

$$\|H_1H_2\|_\infty \leq \|H_1\|_\infty \|H_2\|_\infty$$

holds since $\mathcal{H}_\infty$-norm is an induced norm; however, the same inequality does not hold for the respective $\mathcal{H}_2$-norms. The reason that the $\mathcal{H}_2$-norm is not an induced norm is due to its calculation for a specific set of inputs, as explained below.

Let the stable transfer matrix H have n_i inputs. For $k = 1, \ldots, n_i$, apply the input u_k,

$$u_k(t) := \delta(t)e_k \quad ;$$

($\delta(\cdot)$ denotes the impulse functional and e_k denotes the k-th column of the $n_i \times n_i$ identity matrix). Measure the corresponding outputs y_k, where

$$y_k(t) = (Hu_k)(t) \quad .$$

Compute the individual energies E_k^2, where

$$E_k := \|y_k\|_2 \quad .$$

The $\mathcal{H}_2$-norm of the transfer function H is given by

$$\|H\|_2 = \left(\sum_{k=1}^{n_i} E_k^2\right)^{1/2} \quad .$$

The intuitive explanation is as follows: One by one, apply a white-noise input (spectrum is 1 for all frequencies, hence every mode of the system is excited) and compute the individual energies at the output. The square of the $\mathcal{H}_2$-norm is the sum of these individual energies.

Hence, the $\mathcal{H}_2$-norm is also an energy concept. It reflects the output energy in the presence of wide-band disturbances. The $\mathcal{H}_2$-norm of the open-loop system ($d_{sec} \mapsto y_{los}$ in (18)) is computed as 9.9239 (with a high-pass filter $\frac{s}{s+4\pi}I_2$ cascaded at the input) . The $\mathcal{H}_2$-norm of the closed-loop transfer function from d_{sec} to y_{los} after LAC and HAC (see Figure 21) is computed as 0.2589 , a reduction of 38.33:1 . Simulations were also performed to check against these (analytically) computed values. These are explained within the following subsection.

44

5.4.4 RMS (Root-Mean Square) Values

For a given (one-sided) signal u, the rms (root mean square) value of u is defined as

$$\mathrm{rms}(u) := \left(\lim_{T \to \infty} \frac{1}{T} \int_0^T |u(t)|^2 dt \right)^{1/2} \quad .$$

Note that the square of the rms value of a signal is the average power of the signal. The average is assumed to be taken over a sufficiently large time interval when the integration can not be done analytically. Note that unlike the 2-norm $\|u\|_2$ of u, $\mathrm{rms}(u)$ and u have the same units.

For the final closed-loop system in Figure 21, the maximum real part of the closed-loop eigenvalues is approximately -0.2. Taking a time interval of $T = 30$ seconds (6 times the time constant) and a sampling rate of 200 Hz ($\Delta t = 0.005$), we performed the following simulations:

Using a random number generator, a noise vector w is generated. Under the assumption that the magnitude of the spectrum of w can be approximated by the average of the absolute value of the discrete-Fourier transform of w, we approximated the spectrum of w as constant with magnitude $\alpha = 0.3474$. Approximating the 2-norm of a signal u over T seconds from samples at every Δt seconds, we obtain

$$
\begin{aligned}
\int_0^\infty |u(t)|^2 dt &\approx \int_0^T |u(t)|^2 dt \\
&\approx \sum_{k=1}^{N\Delta t} |u((k-1)\Delta t)|^2 \Delta t \\
&= [\mathrm{norm}(u)]^2 \Delta t \quad ;
\end{aligned}
$$

$\mathrm{norm}(u)$ denotes the euclidean norm of the vector $u \in \mathbb{R}^N$, where N denotes the number of sample points. During simulations, all of the signals are represented by a vector with N entries, hence there is a slight abuse of notation when we express the following approximation in terms of the same variable u:

$$\|u\|_2 \approx \sqrt{\Delta t} \, \mathrm{norm}(u) \quad .$$

In the notation of the previous subsection, we obtain the output vectors y_1 and y_2, corresponding to the inputs $\begin{bmatrix} w \\ 0 \end{bmatrix}$ and $\begin{bmatrix} 0 \\ w \end{bmatrix}$, respectively. Calculating the individual energies E_1 and E_2 as

$$
\begin{aligned}
E_1 &= \mathrm{norm}\left([y_1(:,1); y_1(:,2)]\right) \sqrt{\Delta t}/\alpha = 0.2046 \\
E_2 &= \mathrm{norm}\left([y_2(:,1); y_2(:,2)]\right) \sqrt{\Delta t}/\alpha = 0.1953 \quad ,
\end{aligned}
$$

we obtain a simulation estimate of the $\mathcal{H}_2$-norm as

$$\mathrm{norm}([E_1 \quad E_2]) = 0.2829 \quad ,$$

45

compared to the analytical computation 0.2589 (within 9%). On top of all approximations and possibly not high enough sampling rate, one other source contributing to the mismatch is the noise spectrum. In an $\mathcal{H}_2$-norm computation, it is assumed that every mode is excited by the same magnitude; however, the simulated noise w had apparent magnitude fluctuations.

Approximating the rms value of a time signal u (a vector with N entries, rather) as

$$
\begin{aligned}
[\text{rms}(u)]^2 &\approx \frac{1}{N\Delta t} \int_0^{(N-1)\Delta t} |u(t)|^2 dt \\
&\approx \frac{1}{N\Delta t} \sum_{k=1}^{N} |u((k-1)\Delta t)|^2 \Delta t \\
&= \frac{1}{N}[\text{norm}(u)]^2 \ ,
\end{aligned}
$$

we obtain the following rms ratio from d_{sec} to y_{los} :

$$
\frac{\text{rms}(y1 + y2)}{\sqrt{2}\,\text{rms}(w)} = 0.0122 \ \mu rad/N \ .
$$

In other words, a disturbance d_{sec} with 1 N rms value will cause 12.2 nrad rms deflection at the line-of-sight. Considering the fact that the secondary mirror actuators have a force limit of 8.9 N , this translates into 12.2 nrad rms deflection for 11.23% input disturbance.

Let $P_{y_{los}u_{sec}}$ denote the open-loop transfer matrix from u_{sec} to y_{los} (equivalently, $d_{sec} \mapsto y_{los}$) determined by (18). Let

$$
y := P_{y_{los}u_{sec}} \begin{bmatrix} 1 \\ 1 \end{bmatrix} w \ .
$$

Computing y , we obtain the open-loop (without LAC/HAC) disturbance to line-of-sight rms ratio of

$$
\frac{\text{rms}(y)}{\sqrt{2}\,\text{rms}(w)} = 0.4386 \ \mu rad/N \ ;
$$

hence the LAC/HAC design has achieved an rms reduction of 35.95:1 .

5.5   Robustness of the LAC/HAC Design

Consider the unity-feedback system in Figure 21; C denotes the 34-state compensator obtained by the $\mathcal{H}_\infty$-design and P_{lac} denotes the plant model with low-authority control applied at the primary mirror nodes. The compensator C stabilizes P_{lac} ; however, the major concern is how much plant uncertainty it will tolerate. In other words, if the open-loop transfer function from u_{sec} to y_{sec} is not as determined by (21) (which will definitely be the case due to unmodelled dynamics, uncertainties in the model derivation, etc.) will the compensator C still stabilize this family of plants ? By modeling

the uncertainties, stability robustness margin for each perturbation class determines the admissible perturbations under which the compensator still stabilizes the closed-loop.

In the following subsections we consider four classes of plant perturbations and discuss the associated robustness margins of the closed-loop system in Figure 21 .

5.5.1 Additive Perturbation Margin

Let $P_{\mathrm{lac},y_{\mathrm{sec}}u_{\mathrm{sec}}}$ be the transfer function secondary mirror actuators to the secondary mirror velocity sensors (i.e., $P_{\mathrm{lac},y_{\mathrm{sec}}u_{\mathrm{sec}}} = B_{\mathrm{sec}}^T(sI - A_{\mathrm{lac}})^{-1}B_{\mathrm{sec}}$) . For a given scalar stable transfer function r_{add} , let $B_{r_{\mathrm{add}}}$ denote the set of transfer matrices in (30) .

$$B_{r_{\mathrm{add}}} := \{P_{\mathrm{lac},y_{\mathrm{sec}}u_{\mathrm{sec}}} + \Delta \mid \Delta \text{ is stable and } \bar{\sigma}(\Delta(j\omega)) < |r_{\mathrm{add}}(j\omega)| \text{ for all real } \omega \} .$$
(30)

If C stabilizes $P_{\mathrm{lac},y_{\mathrm{sec}}u_{\mathrm{sec}}}$ then C stabilizes all plants in $B_{r_{\mathrm{add}}}$ if and only if

$$\bar{\sigma}(C(I + P_{\mathrm{lac},y_{\mathrm{sec}}u_{\mathrm{sec}}}C)^{-1}(j\omega)) \, |r_{\mathrm{add}}(j\omega)| \leq 1$$
(31)

for all real ω .

Note that the closed-loop transfer matrix

$$C(I + P_{\mathrm{lac},y_{\mathrm{sec}}u_{\mathrm{sec}}}C)^{-1} = H_{u_{\mathrm{sec}}d_{\mathrm{out}}} \quad ,$$

where $H_{u_{\mathrm{sec}}d_{\mathrm{out}}}$ denotes the stable closed-loop transfer matrix from d_{out} to u_{sec} in Figure 21 . Hence the inverse of the singular-value plot of the closed-loop transfer function from d_{out} to u_{sec} determines the (unstructured) additive perturbation margin as shown in Figure 31.

47

Figure 31:

Admissible additive uncertainty in the transfer matrix from u_{sec} to y_{sec} in Figure 21; i.e., $20\log|r_{add}(j\omega)|$ $[\mu rad/N]$ (see (30)-(31)).

5.5.2 Pre-Multiplicative Perturbation Margin

In this case, suppose that the perturbations (due to uncertainties, unmodeled or neglected dynamics) come in cascade at the plant input. Let $P_{u_{ac},y_{sec}u_{sec}}$ be as in the previous subsection. For a given scalar stable transfer function r_{pre}, let $B_{r_{pre}}$ denote the set of transfer matrices in (32).

$$B_{r_{pre}} := \{P_{u_{ac},y_{sec}u_{sec}}(I + \Delta) \mid \Delta \text{ is stable and } \bar{\sigma}(\Delta(j\omega)) < |r_{pre}(j\omega)| \text{ for all real } \omega\}.$$
(32)

If C stabilizes $P_{u_{ac},y_{sec}u_{sec}}$, then C stabilizes all plants in $B_{r_{pre}}$ if and only if

$$\bar{\sigma}(CP_{u_{ac},y_{sec}u_{sec}}(I + CP_{u_{ac},y_{sec}u_{sec}})^{-1}(j\omega))\,|r_{pre}(j\omega)| \leq 1$$
(33)

for all real ω.

Note that the closed-loop transfer matrix

$$CP_{u_{ac},y_{sec}u_{sec}}(I + CP_{u_{ac},y_{sec}u_{sec}})^{-1} = H_{u_{sec}d_{sec}},$$

where $H_{u_{sec}d_{sec}}$ denotes the stable closed-loop transfer matrix from d_{sec} to u_{sec} in Figure 21. Hence the inverse of the singular-value plot of $H_{u_{sec}d_{sec}}$ determines the pre-multiplicative perturbation margin as shown in Figure 32. Note that the pre-multiplicative perturbation setup is suitable for considering unmodelled actuator dynamics.
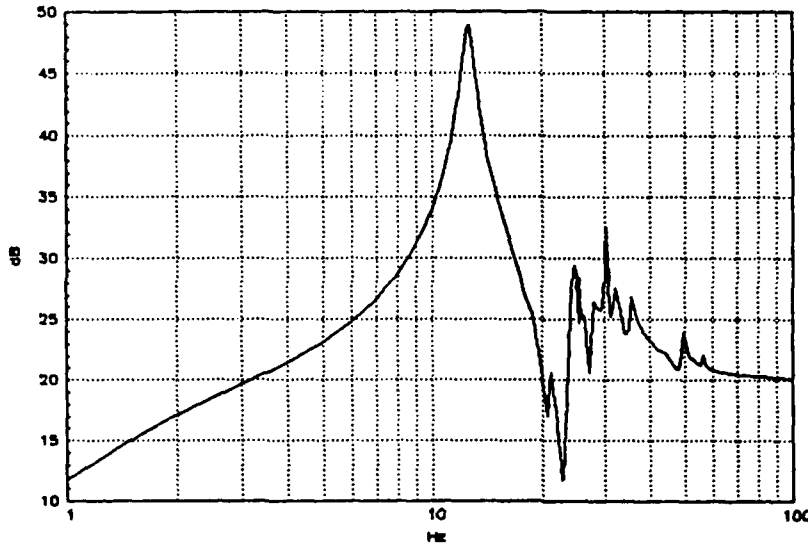
48
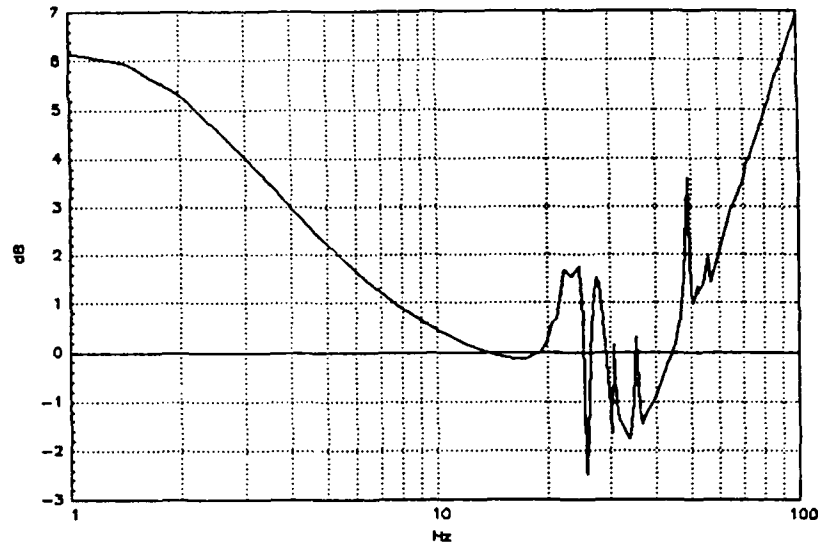
Figure 32:

Admissible pre-multiplicative uncertainty in the transfer matrix from u_{sec} to y_{sec} in Figure 21; i.e., $20\log|r_{pre}(j\omega)|$ (see (32)-(33)).

From Figure 32, we conclude that for frequencies for which the plot is above 0 dB, the actuator uncertainty can be above 100% ; since the minumum is about -2.5 dB, the worst case actuator uncertainty the LAC/HAC design will withstand is $\pm74.99\%$.

The perturbation Δ in (32) is not structured; in our case, it is a two by two stable transfer matrix. The description in (32) may be quite conservative if the actuator uncertainties are decoupled, that is, perturbations are of the form

$$\Delta = \text{diag}[\delta_1 , \delta_2] .$$

In this case, one is interested in the "structured" singular-value of the stable transfer matrix $H_{u_{sec}d_{sec}}$. At any frequency ω , one is interested in the minimum (structured) norm of $\Delta(j\omega)$, such that

$$\det(I + \begin{bmatrix} \delta_1(j\omega) & \\ & \delta_2(j\omega) \end{bmatrix} H_{u_{sec}d_{sec}}(j\omega)) = 0 .$$

Computing this structured perturbation bound, we obtain Figure 33. Note the resemblance to Figure 32.

49
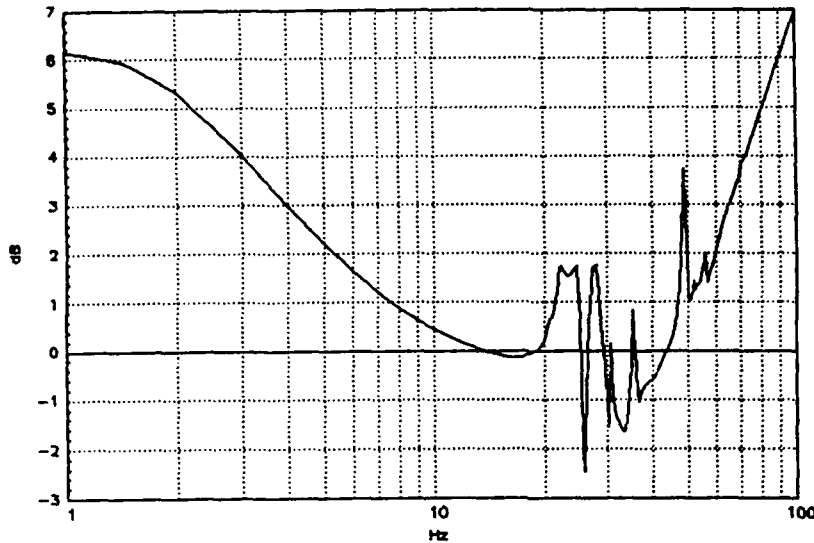
Figure 33:

Admissible multiplicative uncertainty at the secondary mirror actuators provided that
Δ in (32) is diagonal.

In both of the above robustness margin computations, it is assumed that there is no uncertainty in the LAC design. In other words, Figure 32 is the secondary mirror actuator uncertainty bound provided that the LAC gain is precisely $k_{lac} I$. Suppose that we consider the case where the rate-feedback has a pre-multiplicative dynamic uncertainty Δ. Computing the maximum singular-value of the closed-loop (LAC/HAC) transfer matrix that the uncertainty Δ "sees", we obtain the robustness margin in Figure 34.
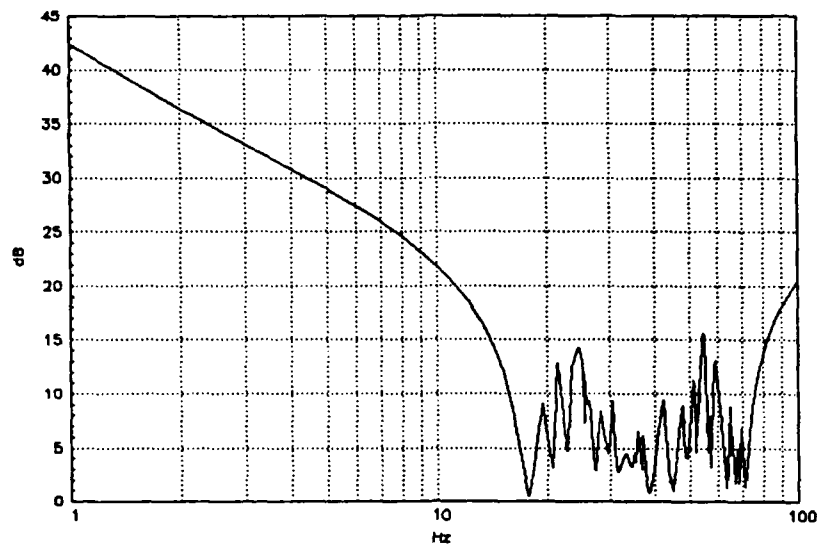
Figure 34:

Admissible pre-multiplicative uncertainty in the LAC rate-feedback provided that there is no secondary mirror actuator uncertainty.

It is interesting to note that the HAC design withstands perturbations in the rate-feedback in the order of 100% ; in other words, the HAC design will still stabilize the plant even if the rate-feedback loop totally fails.

5.5.3   Performance Robustness

The previous subsections addressed the stability robustness of the LAC/HAC design. Provided that the specific class of perturbation is within the associated margin, it is guaranteed that the feedback system remains stable.

In this subsection, we look at the performance degradation of the closed-loop map from d_{sec} in the x-direction to the line-of-sight deflection y_{los} about the y-axis, subject to two cases of uncertainties. For each set of perturbations, the nominal and worst-case Bode plots are obtained. The nominal Bode plot is the closed-loop transfer function from d_{sec} (x-direction) to y_{los} (about y-axis) determined by the system in Figure 21 ; i.e., the associated uncertainty is set to zero. At a given frequency, the worst-case Bode plot determines the worst-case gain when the associated uncertainty is within a specified bound.

Recall that Figure 33 shows the perturbation margin for the structured actuator uncertainty. Suppose that the structured perturbations remain 1 dB lower than the bound in Figure 33 (that is, perturbations can be as high as 89.13% of the stability margin). The corresponding nominal and worst-case Bode plots of the closed-loop map are shown

in Figure 35.

Figure 35:

Nominal (......) and worst-case (——) Bode plots of the closed-loop map (after
LAC/HAC) from d_{sec} (x-direction) to y_{los} (y-direction) provided that the structured
pre-multiplicative plant uncertainties are 1 dB below the margin in Figure 33

52

For the case that the structured perturbations remain 6 dB lower than the bound in Figure 33 (that is, perturbations can be as high as 50% of the stability margin), the corresponding nominal and worst-case Bode plots of the closed-loop map are shown in Figure 36.
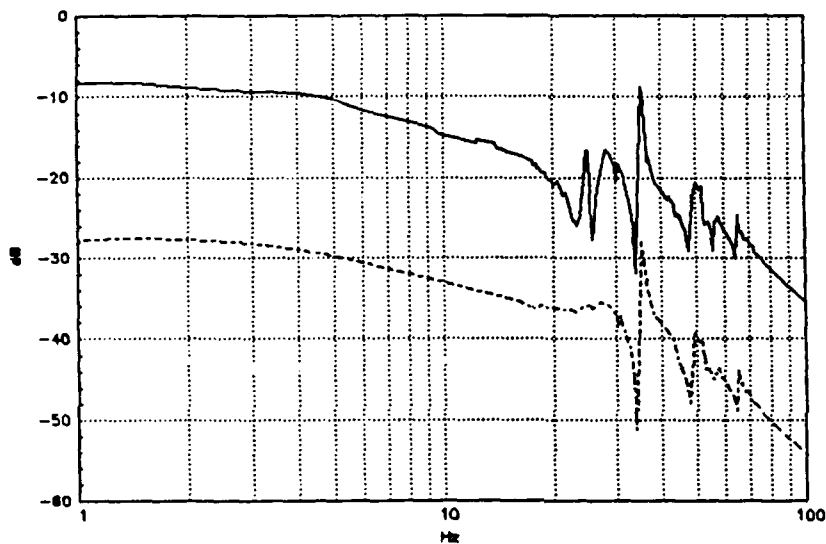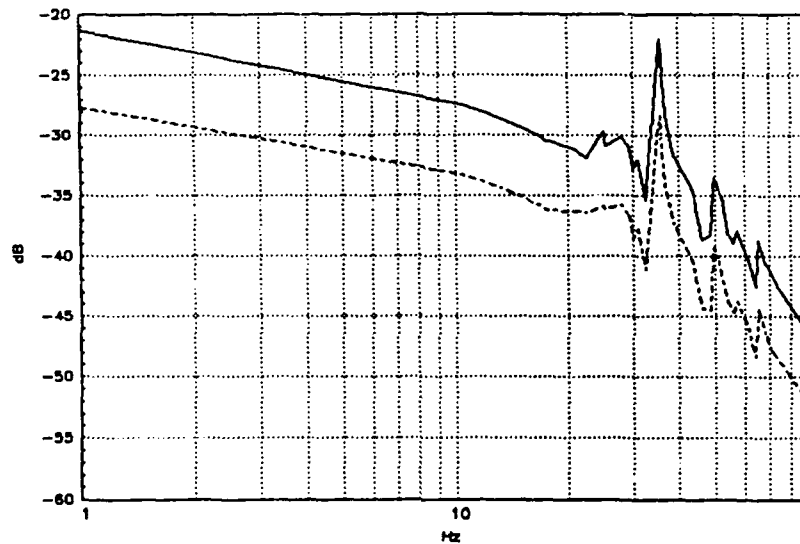

Figure 36:

Nominal (......) and worst-case (———) Bode plots of the closed-loop map (after LAC/HAC) from d_{sec} (x-direction) to y_{los} (y-direction) provided that the structured pre-multiplicative plant uncertainties are 6 dB below the margin in Figure 33.

5.6 Slewing Maneuver Performance

The main point of the LAC/HAC design was attenuation of the secondary mirror actuator disturbance d_{sec} at the line-of-sight output y_{los} . Having achieved this, we now simulate a slewing maneuver about the x-axis, using the primary mirror z-directional thrusters at nodes 1 , 4 , 64 and 67 .

For the given inertia $I_{xx} = 16710\ kgm^2$ and the maximum angular accelaration of $10°/s^2$, using the simplified model

$$I_{xx}\ddot{\theta} = \tau \ , \qquad\qquad (34)$$

we obtain the maximum allowable torque $\tau_{\max} = I_{xx}\pi/18\ Nm$. Applying identical inputs to the thrusters at nodes 1 , 4 in the negative z-direction and 64 , 67 in the positive z-direction simultaneously and taking into account the length of the moment arm ($2.5\ m$), the maximum allowable thrust is $I_{xx}\ \pi/180\ N$. Applying an input of the form

$$u(t) := 224\ \sin(2\pi t/4)(1 - \cos(2\pi t/4))\ N$$

guarantees that the maximum torque is not exceeded; moerover, u does not excite the high-frequency modes of the system (contrary to a bang-bang input signal). For $\tau = 10u$, the plots of u and θ (determined by (34)) are shown in Figure 37.
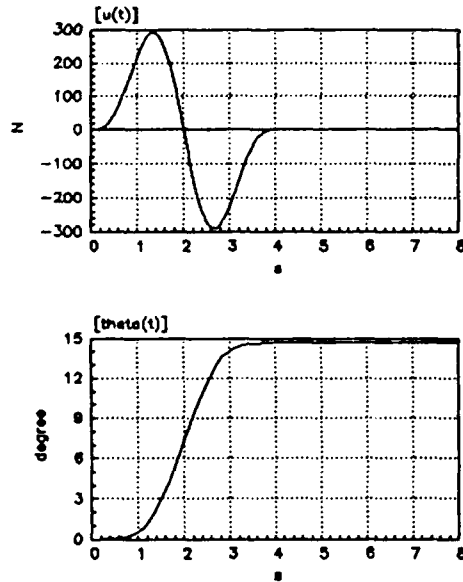
Figure 37:

u and θ plots, where $\ddot{\theta} = \frac{10}{I_{xx}}u$.

5.6.1 Simulation

For the slewing profile mentioned above (approximately $-14.67°$ about the x-axis), the line-of-sight output and the secondary mirror actuator input are plotted in Figure 38.
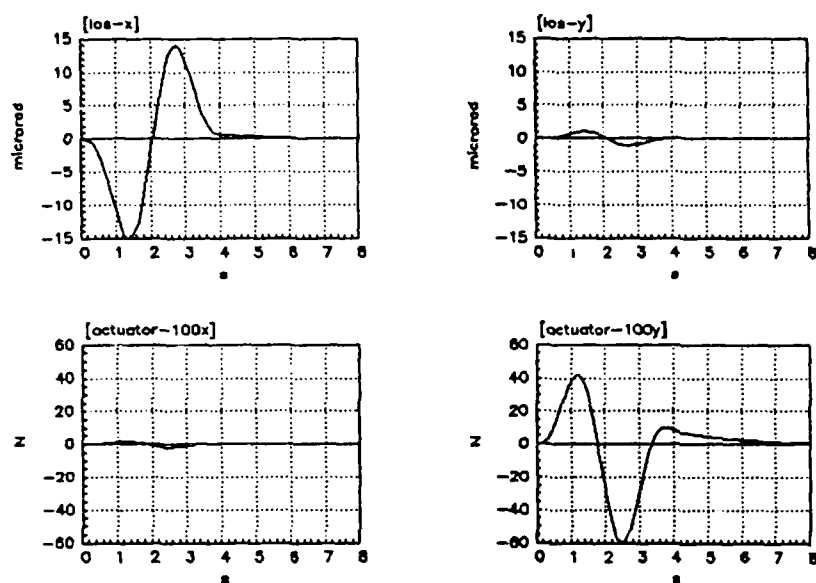
Figure 38:

Closed-loop (LAC/HAC) system responses during the $14.67°$ slew about the x-axis using the primary mirror thrusters at nodes 1 , 4 , 64 and 67 .

Since the actuators at node 100 can exert at most $8.9\ N$, a limiter ($\pm 8\ N$) was cascaded at the compensator output. Figure 39 shows the simulation results with the limiter.

55
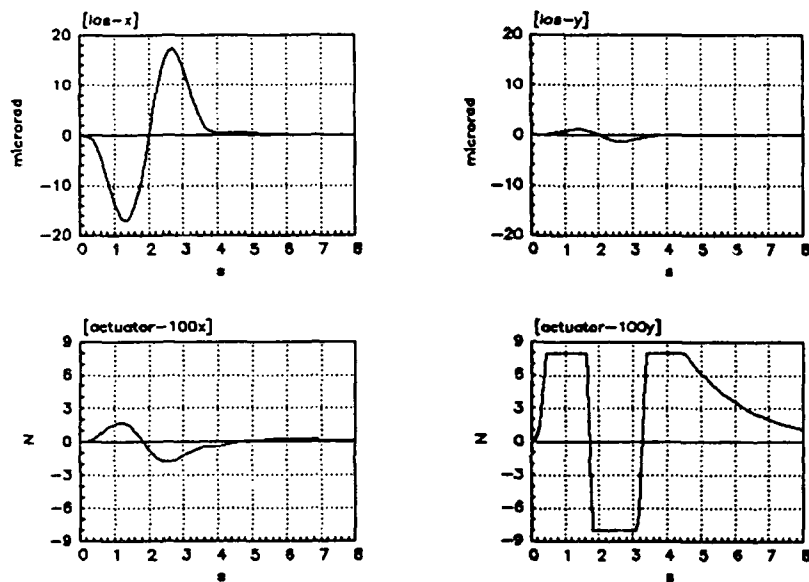
Figure 39:

Closed-loop (LAC/HAC) system responses during the 14.67° slew about the x-axis using the primary mirror thrusters at nodes 1 , 4 , 64 and 67 with ±8 N limiter at the secondary mirror actuator inputs.

6   HAC : With LOS Measurements

In this design, it is assumed that the line-of-sight output y_{los} is measured and can be used in feedback. The same plant descriptions P in (18) and P_{lac} in (21) will be used in the design.

6.1   Disturbance Modeling

Consider the plant model P_{lac} in (21) obtained by applying LAC to P in (18) at the primary mirror nodes (see Figure 17) . As before, there are three sources of disturbances that are considered in the design (see Figure 40):

- The disturbance d_{sec} comes in additively at the secondary mirror actuator inputs (e.g., disturbances due to coolant flow); d_{sec} is assumed to be a wide-band disturbance.

- The output disturbance d_{out} denotes the wide-band sensor noise at the line-of-sight deflection and the secondary mirror velocity measurements.

- The third disturbance d_{thr} is a low-frequency disturbance (up to 2 Hz) due to the z-directional thruster inputs during slewing about the x- and y-axes.

Again, the main objective is to design an output feedback compensator to attenuate the effect of d_{sec} at y_{los} ; the effect of d_{thr} at ylos during slewing is also considered in the design.
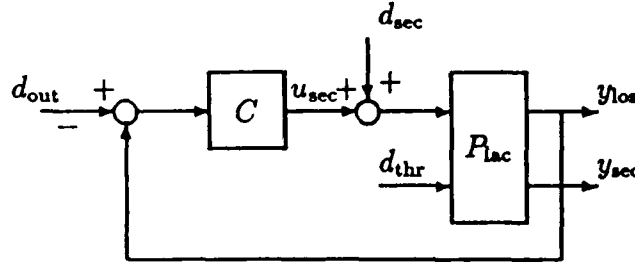

Figure 40: High-authority controller C

6.2   Model Reduction

Consider the plant model P_{lac} in (21) . Without going into any sophisticated model reduction technique or reasoning, an initial design was tried out using a 4-state reduced-order approximation ($\tilde{P}_{lac}$) of P_{lac} obtained by keeping the first two modes (12.2 Hz and 12.6 Hz); the design was satisfactory. Using $MATRIX_X$ notation, $\tilde{P}_{lac}$ is given by:

$$
\tilde{P}_{lac} := \left[\begin{array}{cc} A_{lac}([1\,2\,31\,32],[1\,2\,31\,32]) & B_{sec}([1\,2\,31\,32], :) \quad B_{slew}([1\,2\,31\,32], :) \\ \left[\begin{array}{c} C_{los}(:, [1\,2\,31\,32]) \\ B_{sec}^T(:, [1\,2\,31\,32]) \end{array} \right] & 0 \end{array} \right] . \quad (35)
$$

57

6.3 High-Authority Control Design with LOS Measurements

The $\mathcal{H}_\infty$-design methodology is used to design a dynamic output-feedback compensator from $\begin{bmatrix} y_{los} \\ y_{sec} \end{bmatrix}$ to u_{sec} for the 4-state plant $\tilde{P}_{lac}$ in (35) . For a brief outline of this methodology, refer to Section 5.3.1 .

6.3.1 Augmented Reduced-Order Plant $\tilde{P}_{aug}$

From $\tilde{P}_{lac}$ in (35), we construct the augmented plant $\tilde{P}_{aug}$ with weights $W_1, \ldots, W_5$ as shown in in Figure 41 .
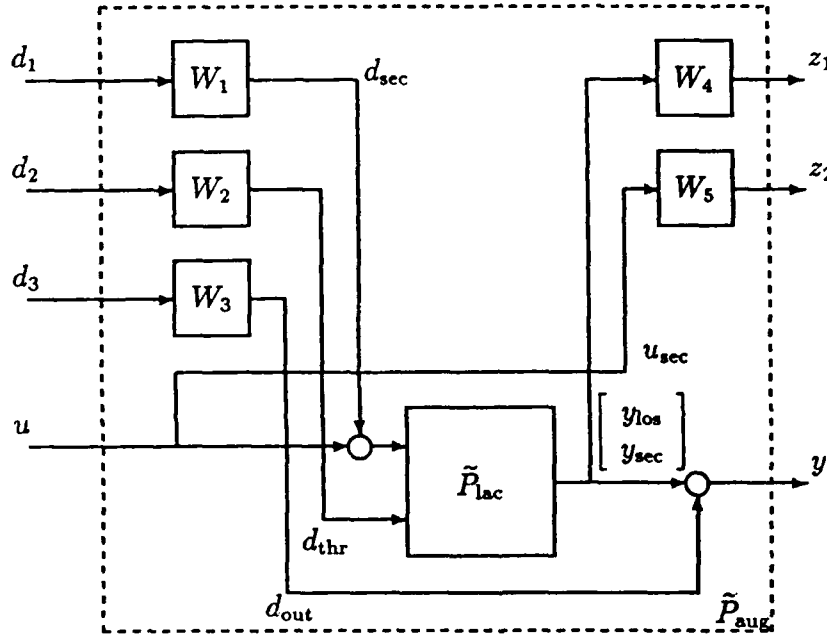
Figure 41: $\tilde{P}_{aug}$ obtained by augmenting the 4-state reduced plant $\tilde{P}_{lac}$

The weights $W_1, \ldots, W_5$ are chosen as follows:

W_1 : $W_1 = I_2$. Since there is no limitation at reducing the DC gain at the line-of-sight (as in the previous rate-feedback design), d_{sec} is assumed to be wide-band.

W_2 : In order not to increase the order of the compensator, initial designs were tried with d_{thr} as a wide-band noise ($W_2 = I_4$). The line-of-sight spec was achieved without increasing the order of the compensator due to the low-frequency description of d_{thr} .

W_3 : The noise intensities at the line-of-sight and secondary mirror velocity measurements. These weights affect the additive-stability margin and the closed-loop

eigenvalue locations. The choice ($W_3 = 0.001\text{diag}[1\ 1\ 5\ 5]$) was a trade-off between faster settling time versus larger additive robustness margin.

W_4 : $W_4 = 1000\,[I_2\ 0]$. If the designed compensator achieves a closed-loop transfer function H_{zd} with $||H_{zd}||_\infty \leq 1$, then the singular-value plot of the closed-loop map from d_{sec} to y_{los} in Figure 40 will be below -60 dB ; an approximate 40 dB peak-to-peak reduction with respect to the open-loop singular-value plot (see Figure 19) .

W_5 : $W_5 = \frac{s+20}{s+200} I_2$. Compared to a constant weight, this specific actuator weight resulted in a better pre-multiplicative robustness margin; the closed-loop map from d_{sec} to u_{sec} rolled-off sooner (thus, the design had a larger stability margin at high frequencies) .

For the augmented plant in Figure 41 , a six-state compensator C is obtained by $\mathcal{H}_\infty$-design where the closed-loop map H_{zd} from d to z in Figure 26 satisfies

$$||H_{zd}||_\infty \leq \gamma = 3 \quad .$$

The choice of γ · as obtained from trial-and-error. Design iterations indicated that the optimal γ (γ_{opt} ;i.e., the least upper bound) is in the interval $(2,3)$.

6.4 Closed-Loop Performance

In this section, we present the performance data for the stable closed-loop system in Figure 40 ; C denotes the six-state compensator obtained by $\mathcal{H}_\infty$-design and P_{lac} denotes the 60-state plant model with low-authority control applied at the primary-mirror nodes (see (21) , Figure 17) .

The maximum singular-value plots of the six transfer matrices (from (d_{sec} , d_{out} , d_{thr}) to (y_{los} , y_{sec})) of the closed-loop system in Figure 40 are shown in Figures 42 and 43 .
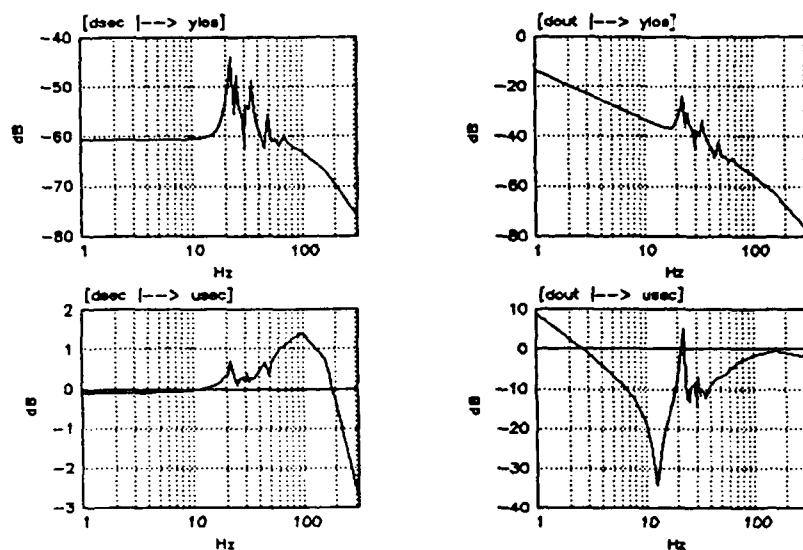
Figure 42:

Singular-value plots of the four transfer matrices $d_{sec} \mapsto y_{los}$, $d_{sec} \mapsto u_{sec}$, $d_{out} \mapsto y_{los}$ and $d_{out} \mapsto u_{sec}$ of the closed-loop (LAC/HAC) system in Figure 40 .
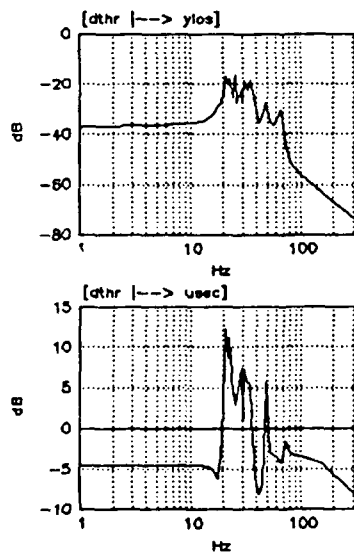
Figure 43:

Singular-value plots of the two transfer matrices $d_{thr} \mapsto y_{los}$ and $d_{thr} \mapsto u_{sec}$ of the closed-loop (LAC/HAC) system in Figure 40 .

60

6.4.1 Disturbance Attenuation at the Line-of-Sight

Let the closed-loop transfer function (after LAC and HAC) from d_{sec} to y_{los} in Figure 40 be denoted by $H_{y_{los}d_{sec}}$. The maximum singular-value plot of $H_{y_{los}d_{sec}}$ is shown in Figure 44 . There is an approximate 40 dB peak-to-peak reduction up to 15 Hz .
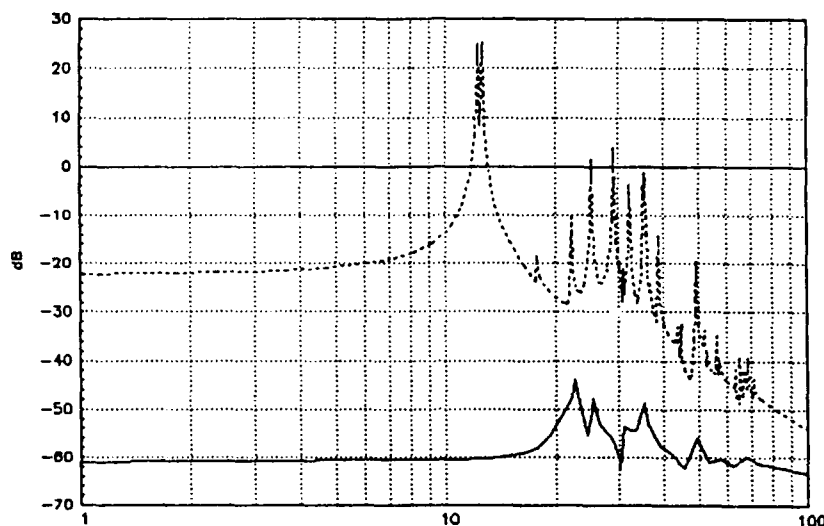
Figure 44:

..... $\bar{\sigma}(C_{los}(j\omega I - A)^{-1}B_{sec})$: open-loop d_{sec} to y_{los} before LAC

—— $\bar{\sigma}(H_{y_{los}d_{sec}}(j\omega))$: closed-loop (after LAC and HAC, see Figure 40) d_{sec} to y_{los}

When the LAC is removed in Figure 40 (i.e., the colocated rate-feedback loop at the primary-mirror nodes is broken), the six-state compensator C still stabilizes the 60-state plant P ; the effect of removing LAC is shown in Figure 45 .

The $\mathcal{H}_2$-norms in Table 3 are computed analytically from the state-space representations of associated transfer matrices.

Table 3: $\mathcal{H}_2$-norms and reduction ratios (with respect to the openloop) for LAC and HAC designs

d_{sec} to y_{los}	$\| \cdot \|_2$ $[\mu rad/N\sqrt{s}]$	reduction
openloop	10.0526	—
lac	2.536	3.96:1
hac/lac	0.025	402:1
hac	0.0541	185:1

61
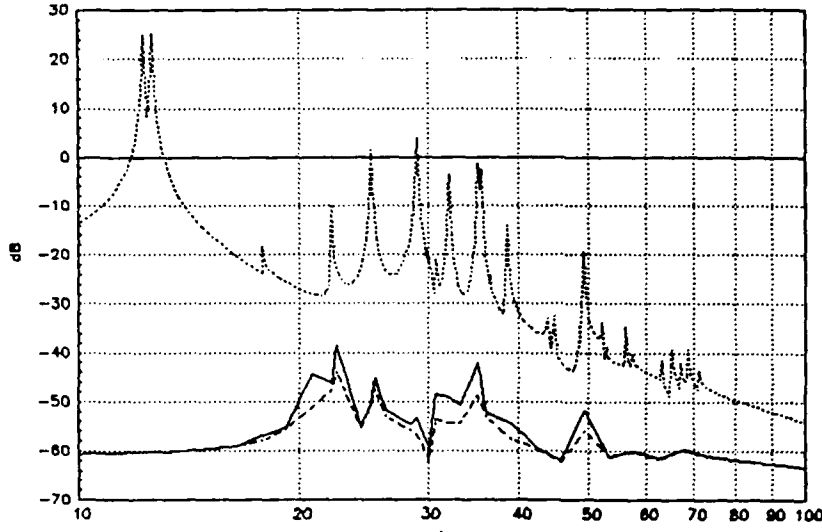
Figure 45:

..... $\bar{\sigma}(C_{\text{los}}(j\omega I - A)^{-1}B_{\text{sec}})$: open-loop d_{sec} to y_{los} before LAC

- - - $\bar{\sigma}(H_{y_{\text{los}}d_{\text{sec}}}(j\omega))$: closed-loop (after LAC and HAC, see Figure 40) d_{sec} to y_{los}

—— $\bar{\sigma}(H_{y_{\text{los}}d_{\text{sec}}}(j\omega))$: closed-loop (HAC only after LAC is removed in Figure 40)

Simulations were performed to check the rms value of the line-of-sight for a simulated noise input. These simulations are now described.

Two 10 sec duration, zero mean, unit variance noise inputs w_1 and w_2 were generated using a sampling interval of 1 ms (hence w_1 , $w_2 \in \mathbb{R}^{10001}$). For the noise vectors generated, the rms value of $\begin{bmatrix} w_1 \\ w_2 \end{bmatrix}$ is computed as 1.4123 N rms; ideally, the rms value would be $\sqrt{2}$ N . Let

$$y_1 := C_{\text{los}}(sI - A)^{-1}B_{\text{sec}}\begin{bmatrix} w_1 \\ w_2 \end{bmatrix} .$$

Note that y_1 denotes the line-of-sight output for the open-loop system (before LAC and HAC) (see Figure 46) . The rms value of y_1 is computed as 210.8 nrad rms . In other words, the open-loop (before LAC and HAC) rms value of the line-of-sight for a 1 N rms disturbance at the secondary mirror actuators is 149.3 nrad rms .

62
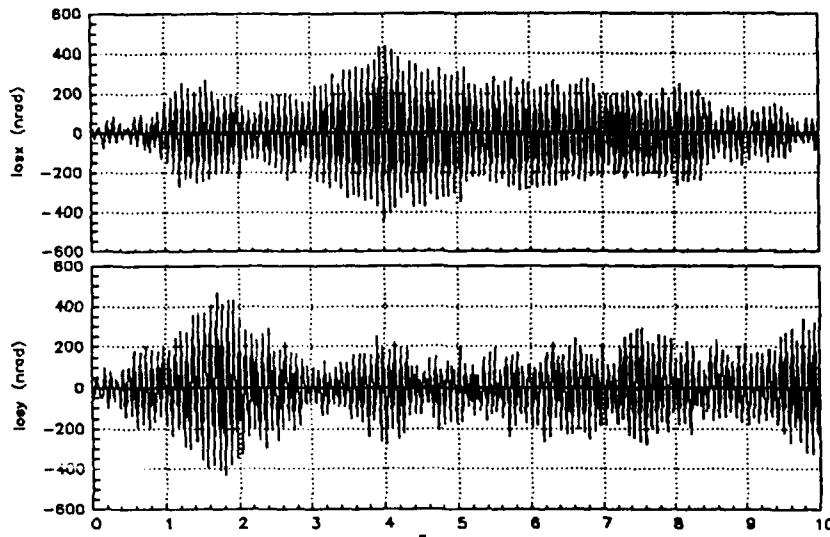
Figure 46:

The line-of-sight responses before LAC and HAC for $d_{sec} = \begin{bmatrix} w_1 \\ w_2 \end{bmatrix}$

Let

$$y_2 := H_{y_{los}d_{sec}} \begin{bmatrix} w_1 \\ w_2 \end{bmatrix} ,$$

where the transfer function $H_{y_{los}d_{sec}}$ denotes the closed-loop map from d_{sec} to y_{los} after LAC and HAC (see Figure 40) . The line-of-sight response of the LAC/HAC system is shown in Figure 47 . The rms value of y_2 is computed as 0.795 nrad rms . In other words, after LAC and HAC (see Figure 40), the rms value of the line-of-sight for a 1 N rms disturbance at the secondary mirror actuators is 0.563 nrad rms (a reduction of 265:1).

63
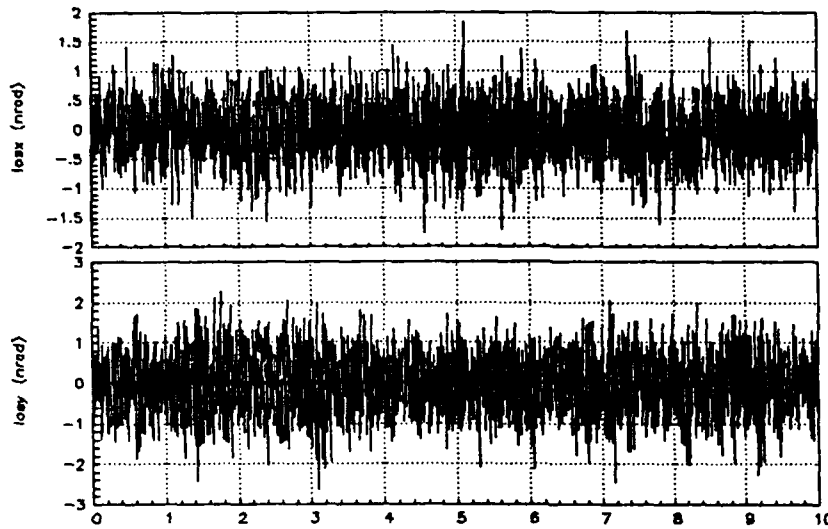
Figure 47:

The line-of-sight responses after LAC and HAC (see Figure 40) for $d_{sec} = \begin{bmatrix} w_1 \\ w_2 \end{bmatrix}$

When the LAC is removed in Figure 40, the closed-loop line-of-sight response y_3 is shown in Figure 48 . The rms value of y_3 is computed as 1.3149 nrad rms . In other words, with HAC only (after LAC is removed in Figure 40), the rms value of the line-of-sight for a 1 N rms disturbance at the secondary mirror actuators is 0.931 nrad rms .

64
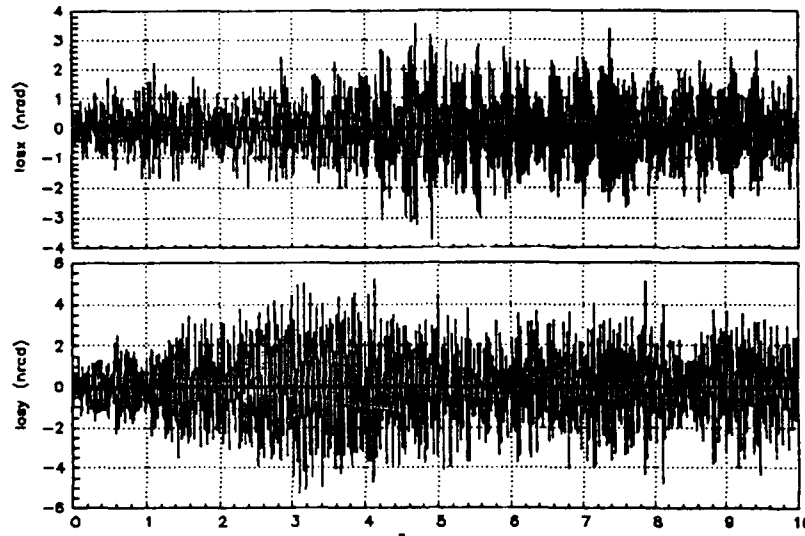
Figure 48:

The line-of-sight responses with HAC only (LAC removed in Figure 40) for $d_{sec} = \begin{bmatrix} w_1 \\ w_2 \end{bmatrix}$

The rms ratios obtained by the simulations mentioned above are summarized in Table 4.

Table 4: rms-ratios obtained by simulation

	$\mathrm{rms}(y_{los})/\mathrm{rms}(d_{sec})$ [nrad/N]
openloop	149.3
lac/hac	0.563
hac	0.931

6.5 Robustness of the LAC/HAC Design

In the following subsections, we consider two classes of plant perturbations and plot the associated robustness margins of the closed-loop system in Figure 40 .

6.5.1 Additive Robustness Margin

The inverse of the maximum singular-value plot of the closed-loop map $d_{out} \longmapsto u_{sec}$ in Figure 40 determines the maximum admissible stable additive perturbation in P_{lac} from u_{sec} to $\begin{bmatrix} y_{los} \\ y_{sec} \end{bmatrix}$. The maximum singular-value plot of the open-loop map

65

$\begin{bmatrix} C_{\text{los}} \\ B_{\text{sec}}^T \end{bmatrix} (sI - A_{\text{lac}})^{-1} B_{\text{sec}}$ is included in Figure 49 for comparison; at a given frequency, the difference gives an idea about the relative contribution of the worst case admissible uncertainty from u_{sec} to $\begin{bmatrix} y_{\text{los}} \\ y_{\text{sec}} \end{bmatrix}$ compared with the worst case gain of the nominal two-input four-output plant P_{lac} .
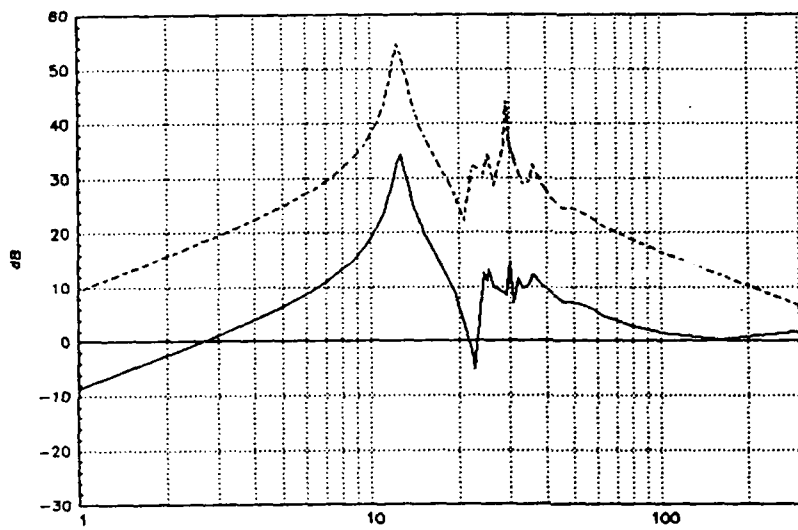
Figure 49:

..... $\bar{\sigma}(\begin{bmatrix} C_{\text{los}} \\ B_{\text{sec}}^T \end{bmatrix} (j\omega I - A_{\text{lac}})^{-1} B_{\text{sec}})$

—— $1/\bar{\sigma}(H_{u_{\text{sec}} d_{\text{out}}}(j\omega))$ where $H_{u_{\text{sec}} d_{\text{out}}}$ denotes the closed loop map from d_{out} to u_{sec} in Figure 40 .

When the LAC is removed in Figure 40 , the six-state compensator still stabilizes the 60-state plant P ; the change in the additive robustness margin when the LAC is removed is shown in Figure 50 .

66
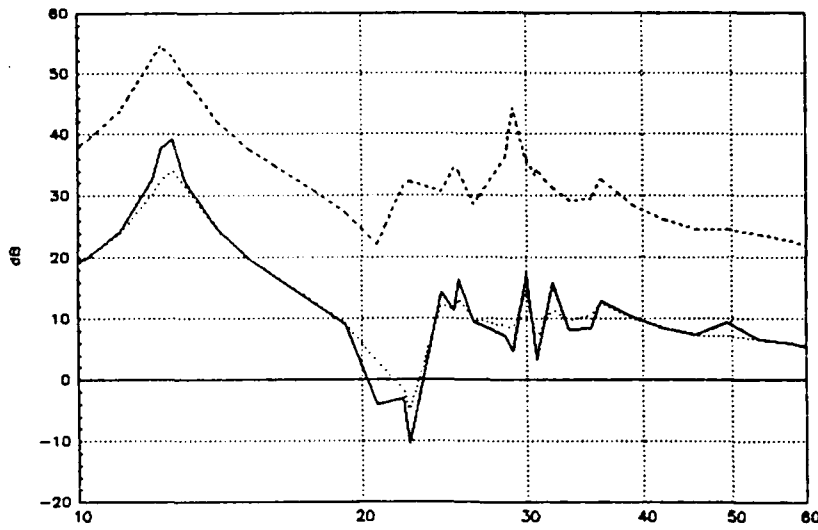
Figure 50:

$$- - - \quad \bar{\sigma}\left(\begin{bmatrix} C_{\text{los}} \\ B_{\text{sec}}^T \end{bmatrix}(j\omega I - A_{\text{lac}})^{-1} B_{\text{sec}}\right)$$

—— $1/\bar{\sigma}(\widehat{H}_{u_{\text{sec}}d_{\text{out}}}(j\omega))$ where $\widehat{H}_{u_{\text{sec}}d_{\text{out}}}$ denotes the closed loop map from d_{out} to u_{sec} in Figure 40 with LAC removed.

. . . $1/\bar{\sigma}(H_{u_{\text{sec}}d_{\text{out}}}(j\omega))$ where $H_{u_{\text{sec}}d_{\text{out}}}$ denotes the closed loop map from d_{out} to u_{sec} in Figure 40 (HAC and LAC) .

6.5.2 Pre-Multiplicative Robustness Margin

The inverse of the maximum singular-value plot of the closed-loop map $d_{\text{sec}} \mapsto u_{\text{sec}}$ in Figure 40 determines the maximum admissible stable pre-multiplicative perturbation at the input of P_{lac} . This margin can be interpreted as the admissible unstructured actuator uncertainty in the HAC/LAC system. From Figure 51, one sees that the margin is below 100% over the band 10 Hz – 200 Hz; worst-case margin is approximately 80% .

67
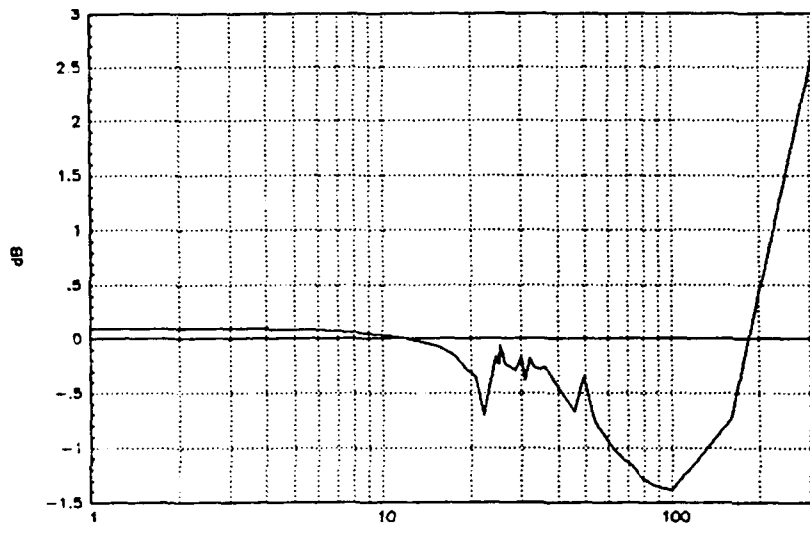
Figure 51:

$1/\bar{\sigma}(H_{u_{\text{sec}}d_{\text{sec}}}(j\omega))$ where $H_{u_{\text{sec}}d_{\text{sec}}}$ denotes the closed loop map from d_{sec} to u_{sec} in Figure 40 .

When the LAC is removed in Figure 40 , the change in the pre-multiplicative robustness margin is shown in Figure 52 .

68
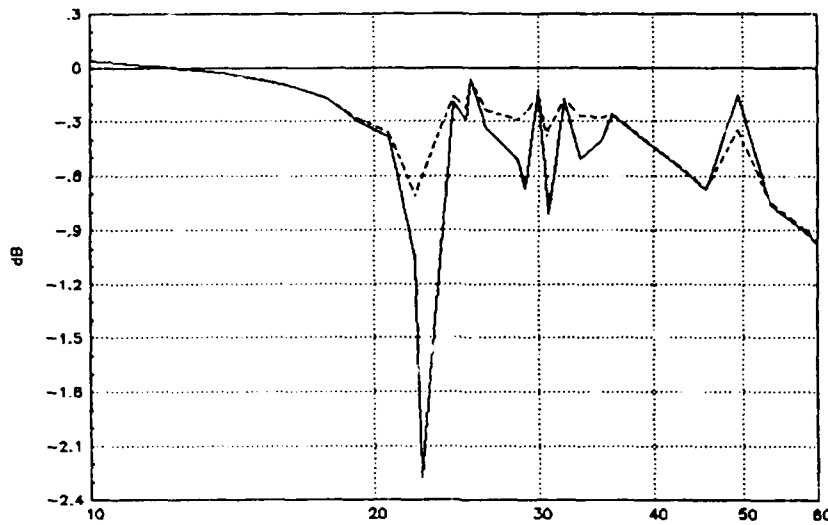
Figure 52:

- - - $1/\bar{\sigma}(H_{u_{sec}d_{sec}}(j\omega))$ where $H_{u_{sec}d_{sec}}$ denotes the closed loop map from d_{sec} to u_{sec} in Figure 40 (HAC and LAC) .

— $1/\bar{\sigma}(\widehat{H}_{u_{sec}d_{sec}}(j\omega))$ where $\widehat{H}_{u_{sec}d_{sec}}$ denotes the closed loop map from d_{sec} to u_{sec} in Figure 40 with LAC removed.

6.5.3 Performance Robustness

The additive and pre-multiplicative robustness margins mentioned in the previous sections are conservative bounds on admissible plant perturbations under which the 6-state compensator still stabilizes the perturbed plant. Provided that the associated class of perturbations are within bounds, the closed-loop system will remain stable; however, the performances other than stabilization may degrade considerably. In order to have an idea on the d_{sec} to y_{los} performance degradation under plant uncertainties, the following worst-case Bode plots are obtained.

Let the pre-multiplicative stable uncertainty be diagonal $\Delta = \text{diag}[\delta_1 \ \delta_2]$; i.e., the actuator uncertainties can be modelled as decoupled. For two levels of uncertainty, the Bode plot of the worst-case actuator-x to line-of-sight-y transfer functions are shown in Figure 53 .

69
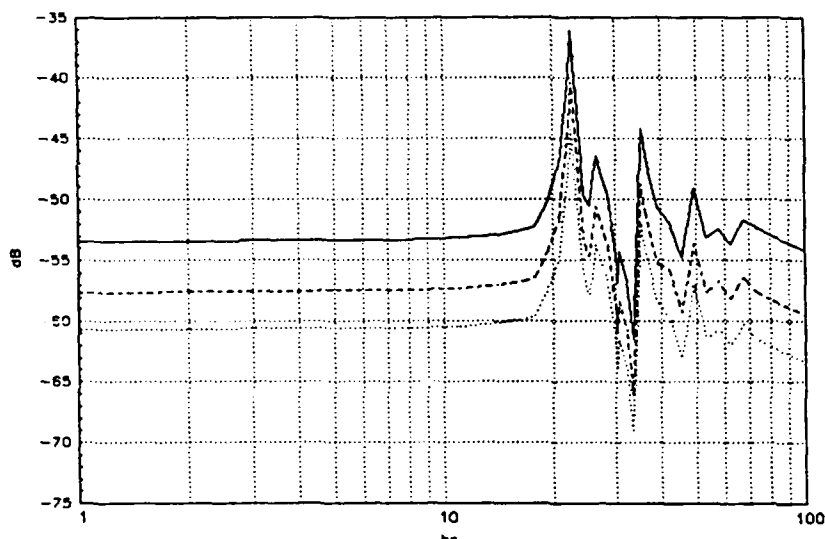
Figure 53:

..... Nominal closed-loop transfer function from d_{sec}-x to y_{los}-y (see Figure 40)

- - - - Worst-case closed-loop transfer function from d_{sec}-x to y_{los}-y provided that the uncertainties δ_1 and δ_2 are uniformly bounded above by -10 dB

—— Worst-case closed-loop transfer function from d_{sec}-x to y_{los}-y provided that the uncertainties δ_1 and δ_2 are uniformly bounded above by -5 dB

70

6.6 Slewing Maneuver Performance

Consider the same slewing maneuver mentioned in Section 5.6 . Applying $-u$ at the z-directional thrusters at nodes 1 , 4 and u at the z-directional thrusters at nodes 64 , 67 yields approximately a negative $15°$ slew about the x-axis (i.e., apply $d_{thr} = \begin{bmatrix} -1 \\ -1 \\ 1 \\ 1 \end{bmatrix} u$

and set all other inputs to zero in Figure 40) . After the slewing inputs are turned off at the fourth second, the line-of-sight and actuator time responses are shown in Figure 54.
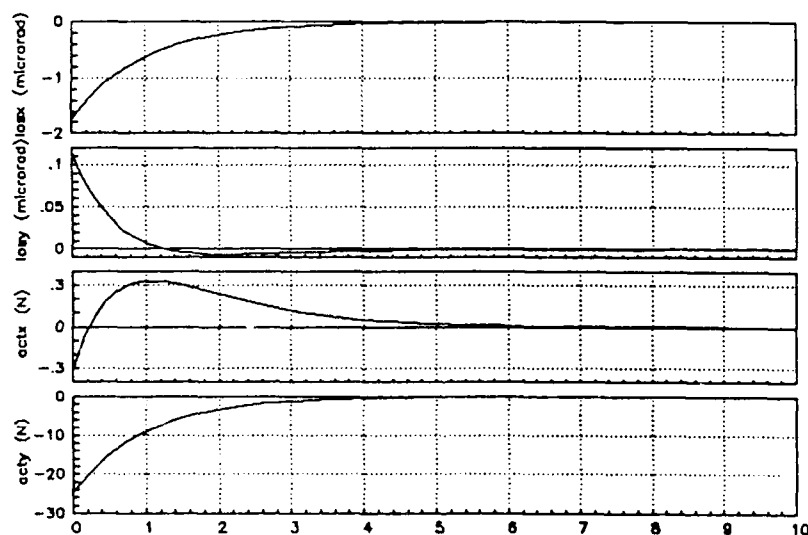
Figure 54:

The line-of-sight and actuator responses (for the LAC/HAC system in Figure 40) after the slewing inputs (d_{thr}) are turned off at the end of 4 s $-15°$ slew about the x-axis.

71

Since the actuators at node 100 can exert at most 8.9 N by assumption (see Section 3.2) , a limiter ($\pm$ 8 N) is cascaded at the compensator output. The simulation results with the limiter are shown in Figure 55 .

Figure 55:

The line-of-sight and actuator responses (for the LAC/HAC system in Figure 40 with a $\pm$ 8 N limiter at the compensator output) after the slewing inputs (d_{thr}) are turned off at the end of 4 s $-15°$ slew about the x-axis.

7 Control Design: Summary and Conclusions

The goal of the two designs in Sections 5 and 6 was to establish the feasibility of achieving disturbance attenuation at the line-of-sight together with a robust feedback controller.
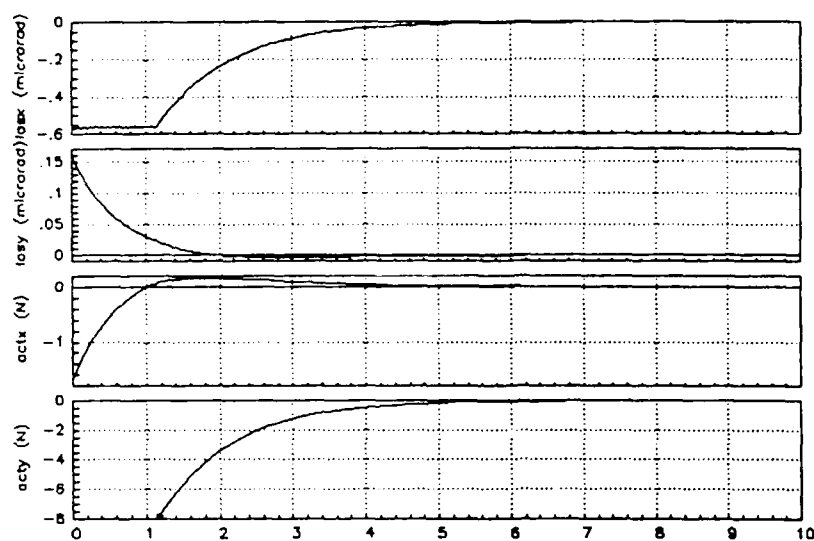
In the first design, the high-authority controller applies colocated rate-feedback at the secondary mirror node 100 . No LOS measurements are available. An $\mathcal{H}_\infty$-design is obtained using a 22-state reduced-order model of the nominal 60-state plant with low-authority control applied at the primary mirror nodes.

In the second design, the line-of-sight measurement was used in feedback. This avoided the limitation on attenuating the DC-gain of the disturbance to the line-of-sight map. An initial $\mathcal{H}_\infty$-design using a 4-state reduced-order model proved satisfactory. Hence a detailed model reduction treatment was skipped for this design.

A detailed discussion of the individual design performances are in Sections 5 and 6 . An immediate comparison may give the impression that the second design is superior to the first; we do not support this argument. The two designs are seperate feasibility studies: after the second design was completed, we did not go back and iterate on the first design to bring it up to the same level of performance as the second one. Moreover. the assumption on measuring the line-of-sight may be unsuitable for the specific application.

For both of the designs, slewing commands at the primary mirror thrusters caused the proof-mass actuators to saturate. The simulations with limited actuators did not show considerable performance degradation. However, attention must be drawn to the closed-loop maps from slewing thruster inputs to the actuators (Figures 29 and 43) . These show considerable amplification (approximately 10 dB) above 20 Hz . No attempt was made to reduce this effect in the design, the assumption being that no signals are at this frequency range.

8 System Identification: Conclusions and Recommendations

8.1 Conclusions

The Phase I study has demonstrated the feasibility of developing system identification tools for control design of a large space structure from measured data, either in a ground-test enviromment or on-orbit.

A fundamental technical issue is to obtain a model estimate which when used in conjunction with some control design procedure would result in acceptable closed-loop performance. In this study the control system was designed using $\mathcal{H}_\infty$ methods. System identification was accomplished using least-squares with filtered data to obtain a nominal model and a frequency domain uncertainty profile which could be used with the control design methods.

The methodologies were tested on a 30 mode simulation model of the ASTREX facility. Representative actuator/sensor types and location were assumed along with a simple mission profile involving disturbance attenuation at the line-of-sight along with a slewing specification.

As a result of this Phase I study, it is clear that several computer-aided design tools are needed in both system identification as well as control design, although in a general way, existing control design tools are further along than existing system identification tools. Nonetheless, we conclude that it is absolutely necessary to have both sets of tools easily available to the user. Several recommendations accrue from this study and these are described in the next section.

8.2 Recommendations

Prior to 1983, all work in system identification for CSI was performed using non-standard custom software or spectral analyzers. Since then a number of tools have emerged for system identification [18,9]. These tools have proven to be very valuable for off-line SISO system identification, but mostly in research environments in the hands of experts in system identification. Outside of this environment they are quite fragile. Thus, it is necessary to develop new tools for dealing with the problem of system identification for control design.

Figure 56 shows the relation of identification and control design. In a sense system identification for control design is a form of model reduction where the data represents the "model" which is reduced to a controller which when applied to the actual system that generated the data would provide acceptable closed-loop performance.

Each path in Figure 56 represents a series of algorithms for which various software tools are required. In particular, the software should perform the functions next described.
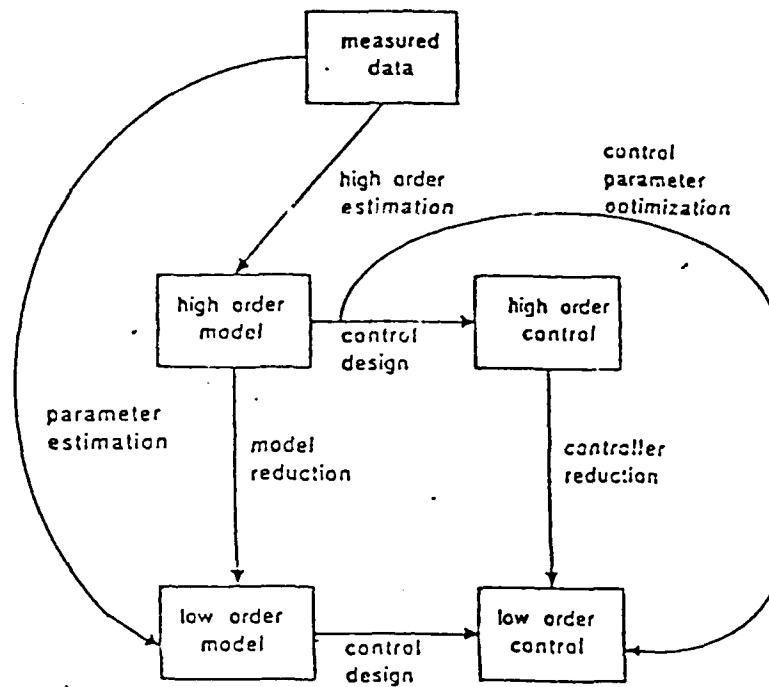
Figure 56: Paths in identification for control design.

Parametric Identification   Parametric methods involve the minimization of some time-domain function of model parameters using an iterative or recursive algorithm. A typical parametric model is a transfer function of fixed order where the coefficients of the numerator and denominator polynomials are the parameters to be estimated. Prediction error models with a least-squares criteria is the standard. Prediction error models arise from a statistical framework and can lead to a Kalman filter or innovations based model. The maximum likelihood method arises from this formulation. However, the formulation can be simply used as a means to obtain a parametric model.

Nonparametric Methods   Non-parametric methods involve the computation of correlation functions and/or their respective spectral densities. A non-parametric model is typically the real and complex values (or gain and phase) of the transfer function at many frequency points. In a sense one can view non-parametric models as high order parametric models. It should be mentioned here that knowledge of the transfer function at many frequency points cannot be directly used for control design. For control one needs the transfer function, so usually non-parametric models have to be transformed to parametric models, usually via parametric methods.

Experiment design   Designing the identification experiment involves many choices, and each choice has a definitive effect on the identified model. These choices include the model structure, probing or test signals, data filters, feedback compensator, criteria of model fit, and computation method. When the intended use of the model is control design, the relations of these choices to the acheivable closed-loop performance can be predicted.

Model Validation Various methods of model evaluation are based on statistical formulations, *e.g.* , maximum likelihood, Cramer-Rao bounds, and confidence tests. These all provide information on the bias and variance of whole classes of estimators, and hence, their primary use is in anylyzing estimation experiments. Some of the procedures can be used on actual data to give an indication of model validity.

Model error estimation To design a high performance control for a flexible space structure it is necessary to have an estimate of model accuracy. Prior information is not sufficient. Several methods exist which can determine model error associated with an identified model from on-orbit data. The model error can be estimted via parameter error estiamtes or via frequency response methods.

Limitations of Current Tools Current software tools, such as $MATRIX_x$, contain primitives which perform some of the above functions, but as already mentioned, are quite fragile in the hands of the non-expert user. Several of these tools have been investigated under Phase I and have proven to be reliable.

Unfortunately, the current tools do not offer the user any guidelines or even provide an easy interface to the expert user. The identification process has to be built up from a few primitives into special purpose macros which only the original user can understand. In addition most of these tools have not been extended for MIMO systems, which is extremely important for CSI problems. Fortunately, many of the necessary lower level tools already exist in some software packages, such as $MATRIX_x$.

The approach we recommend is to encapsulate esisting system identification and control design expertize into new tools so that the non-expert users can gain access to system identification for large MIMO problems typical of CSI as well as to free researchers from time-consuming programming tasks. For example, such tools would also permit on-line identification for CSI by making full use of the already exisiting capabilities of the CDAC (Control and Data Acquisition Computer) on the ASTREX facility at AFAL.

A program to develop these tools should have the following objectives:

- Provide a reliable, repeatable and efficient mechanism for performing system identification for control design.

- Provide an encapsulation of recent advances in system identification for control design in a form useable by normal users.

- Provide a mechanism for rapid transfer of results of on-going research programs to other laboratories and operational programs.

Such a program would result in a set of comprehensive system identification tools for use in the CSI environment. These tools would include off-line and on-line (real-time) capabilities. The user interface would consist of a point-and-click mouse driven workstation based system, both for the off-line and on-line functions. The tools would be part of an

environment that supports system identification and its related functions such as data display, signal processing and test data management. On-line identification algorithms would be easily available and could be tested off-line on a work station and then instantiated in C or Ada code and run in real-time. The tools would be open so that results of new research can be easily integrated into the tools.

The CDAC/ASTREX facility provides a valuable test bed for evaluating and demonstrating these capabilities. As an illustration, Figure 57 shows the overall capabilities of the tools as they would appear in the MATRIX$_X$ environment.

To meet the objectives listed above would require the development of:

- Software primitives for system identification.

- A prototype user-interface to run the primitives.

- On-line system identification algorithms.

All these functions should be designed for compatibility with CDAC and should be tested using the ASTREX facility. These tasks would fulfill the above objectives by providing the user with an interactive interface to aid in the system identification process. The user-interface would facilitate running the necessary primitives or sequence of primitives to perform the identification task. The user- interface encompasses all aspects of system identification including on-line identification and should be able to provide the user with a checklist or even suggestions as to what steps to follow during a session.

Obviously, an important element in the development is the user interface. We envision the interface containing a mouse- oriented set of graphical 'panels'. These panels can display data in custom formats or diagrams, be used to interact with and control ongoing operations, and be extended and customized by experienced users.

Some comments can be made about the panels as envisioned:

- The proposed environment would allow only the operations appropriate at a given time. (For example, loading a system must precede an attempt to simulate it). In the proposed environment, only appropriate operations would be enabled at any given time, and inappropriate operations would not be possible.

- Most normal operations would be outlined in the form of panels which would offer choices. (For example, a plotting panel would allow selection between all the possible plotting choices wih a default shown. This panel would allow entry of labels, etc., so that the user need never enter lower level commands to specify the plotting parameters).

- Choices of operation parameters on panels would be shown only when appropriate and not be visible otherwise. (For example, only after one chooses a bar chart would a bar fill pattern choisc be presented to the user.)

78

- Each panel would offer a screen of 'help' and a continuously updated 'Hints window' to help the user.

Another aspect involves the generation of real-time identification algorithms which are very important for on-orbit testing as well as on-line ground testing. The current CDAC, which uses $MATRIX_x$, is well suited for this task. Real-time algorithms could be generated with CDAC from $MATRIX_x$ block diagrams. The block diagrams can also be instantiated in C or Ada as machine-independent code. Appropriate parametrization allows some degree of cutomization of the on-line algorithm.

Typical on-line algorithms would include:

- Recursive Predection Error (RPE) algorithms for transfer function models.

- Digital filters for data preprocessing.

- Recursive Prediction Error algorithms for state space models similar to an Extended Kalman Filter (EKF).

- On-line non-parametric identification such as correlations, spectra, transfer functions, and coherence functions.

- On-line measures of model error.

The emphasis should be on pratically useful algorithms for MIMO problems typical of CSI. Extensive documentation and user interface shouild be available as this would allow the user to either use a pre-packaged tool or build another suitable template.
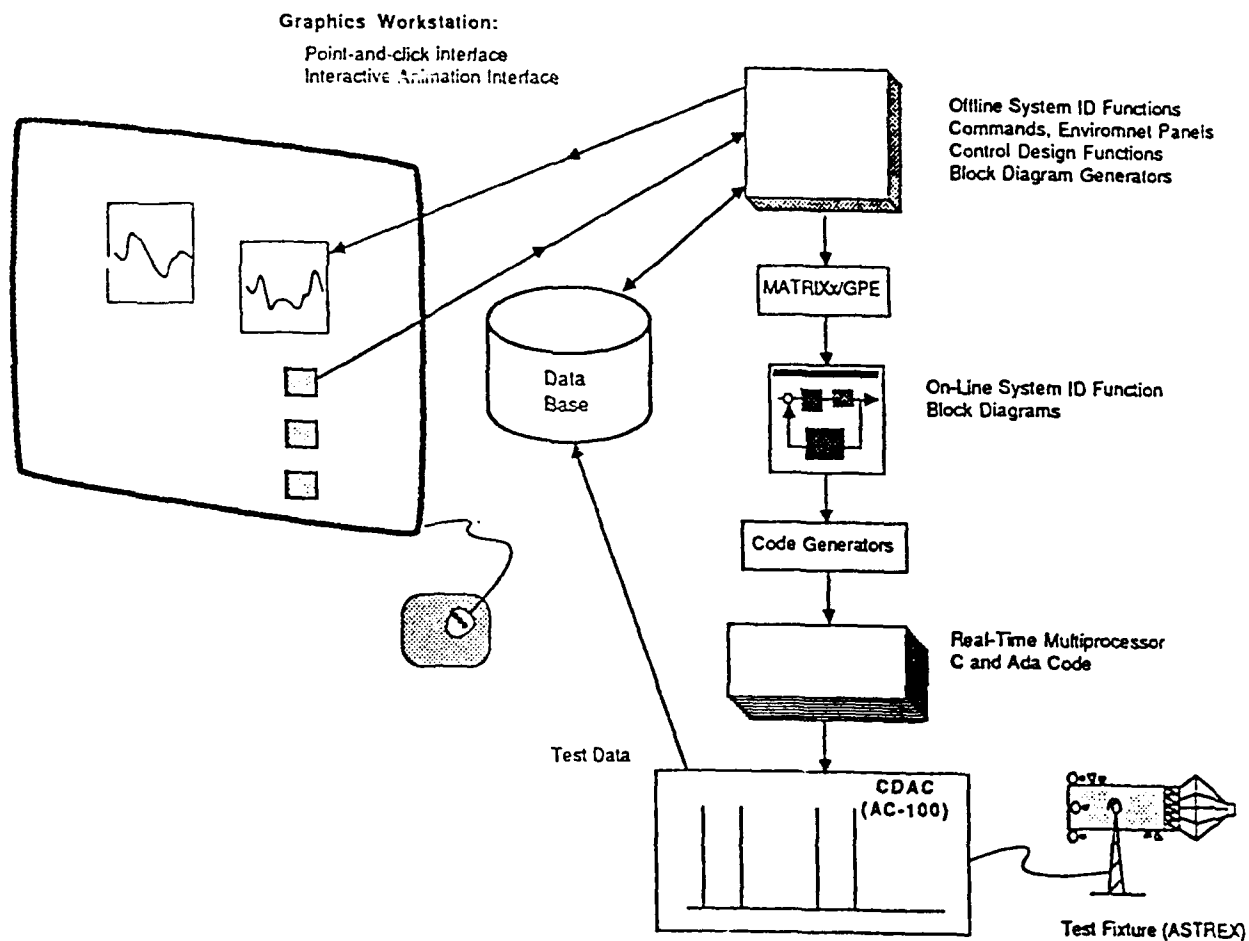
Figure 57: An open environment for system identification and control of large flexible space structures.

Bibliography

[1] "Active Control of Space Structures (ACOSS)," Phase 1A final report, LMSC under DARPA Contract F30602-80-C-0087, Aug. 1981.

[2] "R2P2 Final Report" (1986), prepared by ISI staff for Martin-Marrietta Corp., under Contract GH5-116944.

[3] B.D.O. Anderson, R.R. Bitmead, C.R. Johnson,Jr.,P.V. Kokotovic, R.L. Kosut, I.M.Y. Mareels, L. Praly, and B.D. Riedle (1986), *Stability of Adaptive Systems: Passivity and Averaging Analysis,* MIT Press, 1986.

[4] J.N. Aubrun *et al.*, "Stability augmentation for flexible space structures," *Proc. IEEE CDC*, Hollywood, FL, Dec. 1979.

[5] D.S. Bernstein and D.C. Hyland, "Optimal projection for uncertain systems (OPUS): a unified theory of reduced order robust control design", in *Large Space Structures: Dynamics and Control*, S.N. Atluri and A.K. Amos, editors, Springer-Verlag, 1988.

[6] S. Boyd et al. (1986), "A New CAD Method and Associated Architectures for Linear Controllers", *IEEE Trans. Aut. Control*, AC-33(3):268-283, March 1988.

[7] C. A. Desoer and M. Vidyasagar, *Feedback Systems: Input-Output Properties*, Academic Press, New York, 1975.

[8] J. C. Doyle *et al.*, "State space solutions to standard $\mathcal{H}_2$ and $\mathcal{H}_\infty$ control problems," *IEEE Trans Aut. Control*, vol.AC-34, no.8, pp.831- 847, Aug. 1989.

[9] L. Ljung (1987), *System Identification: Theory for the User*, Prentice Hall, New Jersey.

[10] L. Ljung and T. Soderstrom, *Theory and Practice of Recursive Identification*, MIT Press, Cambridge MA.

[11] S.D. McIntosh and M.A. Floyd, "Investigation of interactive structural and controller synthesis for large spacecraft," final report under AFOSR Contract F49620-84-C-0025.

[12] S. Morrison, Y. Ye, C.Z. Gregory, R.L. Kosut, and M. Regelbrugge, "Integrated structural/controller optimization of large space structures," *Proc. AIAA Guid. and Control Conf.*, no. AIAA-88-4305-CP, Minn., MN, Aug. 1988.

[13] M.Vidyasagar (1985), *Control System Synthesis: A Factorization Approach*, MIT Press, Cambridge, MA, 1985.

[14] Y. Ye and E. Tse (1988), "An extension of Karmarkar's projective algorithm for convex quadratic programming," to appear, *Math. Programming*.

[15] G. Zames (1980), "Feedback and optimal sensitivity:model reference transformations,multiplicative seminorms and approximate inverses," *IEEE Trans Aut. Control*, Vol AC-26, pp. 301-320, April 1981.

[16] D.R. Brillinger(1975), *Time Series: Data Analysis and Theory*, Holt, Rinehart, and Wintron, New York.

[17] J.C. Doyle and G. Stein (1981), "Multivariable Feedback Design: Concepts for a Classical/Modern Synthesis," *IEEE Trans. Automat. Contr.*, Feb. 1981.

[18] S. Shah and R. Walker (1985), "System Identification Module," in *MATRIX$_x$ User's Guide*, ISI.

[19] K.J. Astrom and P. Eykhoff (1971), "System identification- a survey," *Automatica*, vol.7, pp.123-167.

[20] R.L. Kosut (1986), "Adaptive Calibration: An Approach to Uncertainty Modeling and On-Line Robust Control Design," *Proc. 25th IEEE CDC*, Athens, Greece, Dec. 1986.

[21] R.L. Kosut (1987), "Adaptive Uncertainty Modeling: On-Line Robust Control Design," *Proc. 1987 ACC*, Minneapolis, MN, June 1987.

[22] R.L. Kosut (1988), "Adaptive Robust Control via Transfer Function Uncertainty Estimation", *Proc. 1988 ACC*, Atlanta, GA, June 1988.

[23] R. LaMaire *et al.*(1987), "A frequency domain estimator for use in adaptive control systems," *Proc. 1987 ACC*, Minn, MN, pp.238-244, June.

[24] G.M. Jenkins and D.G. Watts (1968), *Spectral Analysis and Its Applications*, Holde-Day, San Francisco.

[25] L. Ljung (1985), "On the Estimation of Transfer Functions," *Automatica*, **21**(6), Nov. 1985.

[26] S. Morrison and B. Walker (1988), "Batch-least-squares adaptive control in the presence of unmodeled dynamics," *Proc 1988 ACC*, Atlanta, GA., June 1988.

[27] M.B. Priestly (1981), *Spectral Analysis and Time Series*, Academic Press, New York.

[28] H. Cramer, *Mathematical Methods of Statistics*, Princeton University Press, 1946.

[29] C. Z. Gregory Jr. , "Reduction of Large Flexible Spacecraft Models Using Internal Balancing Theory," *Journal of Guidance*, vol. 7, no. 6, pp. 725-732, Nov.-Dec. 1984.

[30] M. G. Safonov, R. Y. Chiang and H. Flashner, " $\mathcal{H}_\infty$ Robust Control Synthesis for a Large Space Structure," *Proc. American Control Conference*, pp. 2038-2045, Atlanta, Georgia, 1988.